*electronics*

MDPI

*Article*

# Experimental Implementation of a Second-Order Adaptive Fuzzy Logic Controller for PMSG-Based Wind Energy Conversion Systems

**Basem E. Elnaghi [1,*], Hala Samy Sayed Abdelhafez [2], Mohamed M. Isamail [3] and Ahmed M. Ismaiel [1]**

[1] Electrical Power and Machines Department, Faculty of Engineering, Suez Canal University, Ismailia 41522, Egypt; pgs.027636625@eng.suez.edu.eg
[2] The British School Al Khubairat, Abu Dhabi 4001, United Arab Emirates; hsamysayedabdelhafez12@britishschool.sch.ae
[3] Electrical Engineering Department, Faculty of Engineering, Helwan University, Cairo 11795, Egypt; dr.mohamed@h-eng.helwan.edu.eg
* Correspondence: basem_elhady@eng.suez.edu.eg

**Abstract**

This study presents a second-order adaptive fuzzy logic controller (SO-AFLC) to enhance the dynamic performance of permanent magnet synchronous generator (PMSG)-based wind energy conversion systems (WECSs). The proposed controller simultaneously performs maximum power point tracking (MPPT), DC-link voltage regulation, and reactive power control and minimizes speed-tracking errors. Its performance is evaluated under step-changing wind conditions and measured wind speed data from Ras Gharib, Gulf of Suez, Egypt. A comprehensive comparison with conventional proportional-integral (PI) and adaptive fuzzy logic controller (AFLC) methods is conducted using MATLAB/Simulink. Compared with the AFLC and PI controllers, the proposed SO-AFLC achieves superior rotor speed tracking performance, with improvements of 36.98% and 53.26%, respectively. The proposed controller is further validated experimentally using a dSPACE DS1104 real-time platform. Additionally, an overall Integral Absolute Error (IAE)-based wind performance index is introduced to enable an objective comparison of the investigated controllers under identical operating conditions. SO-AFLC decreases the average of IAEs by 9.15% and 21.36% compared with the AFLC and PI controllers, respectively. Both simulation and experimental results demonstrate that the SO-AFLC provides faster transient response, higher tracking accuracy, and more reliable energy conversion, making it a promising solution for improving the grid integration of PMSG-based WECSs.

**Keywords:** second-order adaptive fuzzy logic controller; grid-connected wind energy conversion system; reactive power control; maximum power point tracking

Check for updates

Academic Editor: Ahmed Abu-Siada

Received: 4 August 2026
Revised: 15 September 2026
Accepted: 17 September 2026
Published: 19 September 2026

**Copyright:** © 2026 by the authors. Licensee MDPI, Basel, Switzerland. This article is an open access article distributed under the terms and conditions of the Creative Commons Attribution (CC BY) license.

## 1. Introduction

The rapid growth in global energy demand and increasing environmental concerns have intensified the transition from conventional fossil-fuel-based energy systems to sustainable and renewable energy technologies. While petroleum-based fuels continue to be prevalent in the transport industry, they are largely responsible for increased greenhouse gas emissions, climate change, and environmental pollution. Furthermore, increased prices of fuel oil, shortages of fossil fuel reserves, and energy security issues have led to efforts geared at developing cleaner energy alternatives. Various types of renewable energy

technologies exist, but wind power is a particularly intriguing alternative owing to its availability, technological readiness, competitiveness in terms of cost of production, and zero environmental impact during the process of production. Within the last ten years, improvements in wind turbine and power electronic converter technology have greatly increased the performance of modern wind energy conversion systems (WECS). Nowadays, power electronics converters have become an integral part of wind plants that are connected to electricity grids. Consequently, recent advances in converter technology have played a fundamental role in improving the overall operational performance and grid integration capability of wind generation systems [1–3]. Modern wind turbines are generally classified into fixed-speed, semi-variable-speed, and fully variable-speed configurations according to their generator and converter arrangements. Fixed-speed wind turbines, which were widely adopted in early wind farms, have gradually become obsolete because of their limited operating flexibility, high mechanical stress, and poor grid support capability. In contrast, variable-speed wind turbines (VSWTs) provide superior energy capture, lower mechanical loading, improved power quality, and enhanced compliance with modern grid codes. These advantages have established variable-speed technology as the preferred solution for contemporary large-scale wind power plants [4,5]. Numerous generator topologies have been investigated for variable-speed wind energy conversion systems, with considerable attention devoted to improving system dynamics, power quality, and grid integration capability [5–8]. Existing approaches include energy storage system (ESS) integration, pitch angle control (PAC), and advanced voltage source inverter (VSI) control techniques [8–10]. Even though pitch angle control ensures proper regulation of mechanical power from the wind, the relatively slower reaction time limits its ability to react quickly to fast changes in the speed of wind or grid. Energy storage systems may help to provide better flexibility and power management; however, the cost involved in installation and maintenance hinders wider implementation of such systems. Consequently, control strategies based on voltage source converters have attracted considerable research interest because they provide fast dynamic response, high control accuracy, and cost-effective implementation. Among the available VSC control methods, cascaded control schemes (CCSs) have become one of the best widely adopted approaches for grid-connected WECSs because of their modular architecture, straightforward implementation, and robust control performance [8,11]. Conventional PI controllers remain the most commonly employed regulators within CCS structures owing to their simplicity and ease of practical implementation [6,12]. More recently, fuzzy logic controllers (FLCs) have emerged as an attractive alternative because they can effectively handle nonlinear system characteristics and parameter uncertainties while improving transient performance [11,13]. Nevertheless, maintaining high control accuracy and robust performance under rapidly changing wind conditions, system nonlinearities, and external disturbances continues to represent a significant challenge. Therefore, there is a growing need for advanced intelligent control strategies capable of simultaneously improving energy extraction efficiency, system stability, dynamic response, and compliance with modern grid requirements. The operating characteristics of a VSWT, shown in Figure 1 [14], can be divided into four distinct operating regions according to wind speed. When the wind speed is below the cut-in threshold, the turbine remains inactive and no electrical power is generated. The second operating region corresponds to the MPPT mode, where the control system maintains the optimal operating condition by regulating the electromagnetic torque while keeping the blade pitch angle constant to maximize energy capture. When the speed of wind rises over the rated value, the turbine enters the third operating region, where pitch angle control is activated to maintain constant rated power. Finally, when the wind speed surpasses the cut-out limit, the protection system disconnects the turbine from operation to prevent mechanical and electrical damage [15,16]. Since

the primary objective of this work is to optimize energy harvesting, the proposed control strategy focuses exclusively on the MPPT operating region.

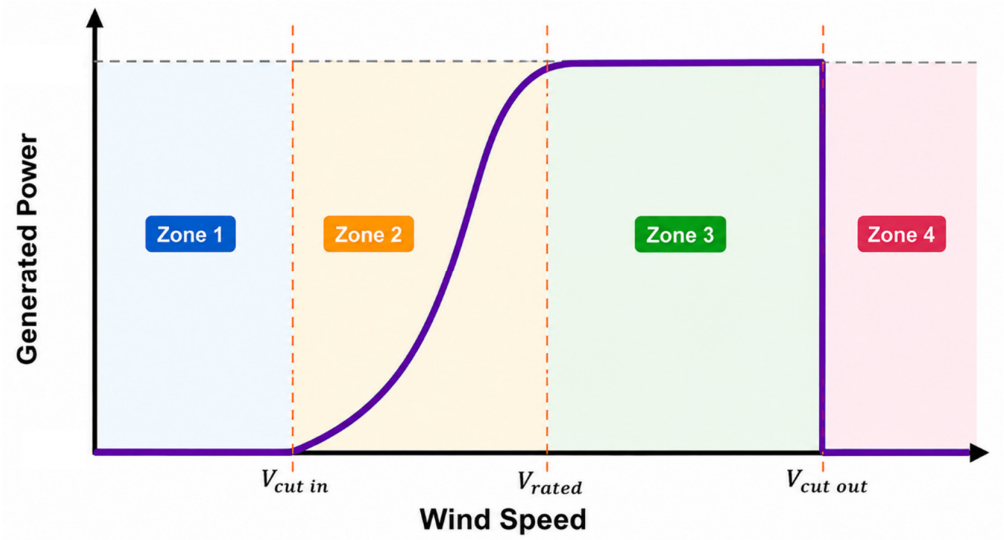



**Figure 1.** Wind speed curve.

Despite the extensive use of conventional PI and AFLC in WECSs, relatively few studies have investigated the application and practical investigation of SO-AFLCs. In particular, comprehensive comparisons between SO-AFLC and well-established control approaches under both simulation and real-time operating conditions remain scarce. This lack of experimental evidence motivates further investigation into the potential advantages of second-order adaptive control techniques for modern wind energy systems. The PI controller continues to be the preferred solution in many industrial applications because of its simple structure, low computational complexity, and ease of implementation. Under nominal operating conditions, PI-based controllers generally provide satisfactory stability and acceptable steady-state performance. Nevertheless, their effectiveness deteriorates when the system exhibits strong nonlinear characteristics, parameter uncertainties, or rapidly changing external disturbances, which are common features of practical wind energy conversion systems [9,17]. These limitations often result in degraded tracking accuracy and slower dynamic response. To improve controller adaptability under nonlinear operating conditions, adaptive fuzzy logic controllers have received considerable attention in recent years [18–20]. By integrating fuzzy inference with adaptive parameter tuning, AFLCs are capable of modifying their control actions according to system behavior without requiring an accurate mathematical model. This feature enables improved disturbance rejection, enhanced robustness against parameter variations, and superior transient performance compared with conventional PI controllers. Consequently, AFLCs have become an attractive intelligent control solution for renewable energy applications. Several researchers have reported the successful application of adaptive fuzzy control in PMSG-based wind turbines. Previous studies have demonstrated that AFLC can improve MPPT, increase robustness during wind speed variations, and enhance the dynamic behavior of grid-connected systems [18–20]. Nevertheless, most of these investigations rely primarily on numerical simulations, whereas experimental verification using real-time digital control platforms or hardware-in-the-loop testing remains relatively limited [20–24].

Soliman et al. [25] proposed an AFLC strategy to enhance the operational performance of grid-tied PMSG-based WECSs. Their results confirmed the ability of adaptive fuzzy control to enhance energy conversion efficiency under variable operating conditions. Similarly, Farag et al. [26] investigated intelligent yaw control techniques for large-scale wind

turbines to improve rotor alignment with the incoming wind direction, thereby maximizing energy capture while reducing structural loading. Other studies have mainly concentrated on improving MPPT performance under fluctuating wind conditions [27]. Although these contributions demonstrated the advantages of AFLC, they were generally evaluated under limited operating scenarios and provided only a brief discussion of computational complexity, scalability, long-term robustness, and performance during severe grid disturbances. Likewise, the adaptive hybrid virtual inertia controller proposed in [28] primarily focused on frequency support enhancement, leaving several practical implementation issues insufficiently addressed, particularly those related to large-scale wind farms and continuously varying wind conditions. Recent developments in intelligent control have further demonstrated that fuzzy-based strategies outperform conventional PI controllers in renewable energy applications characterized by nonlinear dynamics and uncertain operating environments. AFLCs have been successfully utilized for photovoltaic systems, distributed generation units, robotic manipulators, and grid-connected renewable energy systems, consistently providing improved tracking accuracy, disturbance rejection capability, and operational robustness [29–34]. These studies confirm the effectiveness of adaptive fuzzy control in handling complex nonlinear systems where conventional linear controllers often experience degraded performance. Despite these achievements, conventional AFLC structures may still suffer from limited adaptation capability and relatively slow convergence under highly dynamic operating conditions. To address these shortcomings, second-order adaptive fuzzy logic controllers have recently emerged as an advanced alternative. Experimental investigations reported in [35,36] have demonstrated that second-order adaptive fuzzy logic control (SO-AFLC) can achieve faster transient responses, enhanced disturbance rejection, and improved robustness compared with conventional PI and adaptive fuzzy logic controllers (AFLCs) in semi-variable-speed wind energy conversion systems based on doubly fed induction generators (DFIGs). In such configurations, the DFIG typically operates within a limited speed range around the synchronous speed, commonly around $\pm$30%, allowing the power electronic converter to be rated at only a fraction of the machine capacity. This configuration reduces converter power requirements while retaining effective variable-speed operation. Nevertheless, the applicability of SO-AFLC to full-scale variable-speed wind energy conversion systems based on PMSGs, in which the entire generated power is processed through the power-electronic conversion stage, remains comparatively underexplored. In particular, comprehensive investigations that combine detailed numerical analysis with real-time experimental validation under both abrupt and realistic wind-speed variations are still limited. Motivated by this gap, the present study investigates the application and real-time implementation of SO-AFLC for a grid-connected PMSG-based wind energy conversion system. The proposed control framework integrates the adaptive nonlinear compensation capability of AFLC with a second-order sliding-mode correction mechanism to enhance parameter adaptation and transient regulation under rapidly varying operating conditions. The resulting controller is systematically evaluated against conventional PI and AFLC strategies in terms of maximum power point tracking, dynamic response, disturbance rejection, and overall regulation performance.

The principal contributions of this study are summarized as follows:

1. Comprehensive simulation and experimental validation: The performance of the suggested SO-AFLC for a PMSG-based wind power plant is evaluated through detailed simulation in MATLAB/Simulink 2026a and practical experimental implementation using the dSPACE DS1104 control kit.
2. Unified performance assessment framework: An Integral Absolute Error (IAE)-based evaluation framework is developed to provide a consistent and objective comparison of SO-AFLC, AFLC, and PI controllers under identical operating conditions.

3. Validation using real wind data: The proposed control strategy is experimentally validated using measured wind speed data obtained from a wind farm in the Ras Ghareb, demonstrating its practical applicability and improved dynamic performance compared with conventional control approaches.

Overall, this study validates the effectiveness of the proposed SO-AFLC for PMSG-based wind energy conversion systems, demonstrating its potential to improve system performance and support the development of sustainable energy technologies for practical applications. The remainder of this paper is organized as follows. Section 1 presents the introduction and a review of the relevant literature. Section 2 describes the mathematical modeling of the proposed system. Section 3 discusses the simulation results and performance evaluation. Section 4 details the implementation and operating principles of the dSPACE DS1104 real-time control platform. Section 5 presents the experimental validation and analyzes the corresponding results. Finally, Section 6 summarizes the key findings and outlines recommendations for future research.

## 2. The Configuration of a PMSG-Based Wind Power Plant

The overall configuration of the grid-connected PMSG-based wind energy conversion system investigated in this study is illustrated in Figure 2. The proposed system consists of a VSWT mechanically coupled to a permanent magnet synchronous generator (PMSG). The generated electrical power is processed through a back-to-back power conversion stage comprising a machine side converter (MSC) and a grid-connected converter (GCC) interconnected by a DC-link capacitor. This arrangement enables efficient power transfer, independent regulation of the generator and grid interfaces, and steady performance in a variety of wind situations.

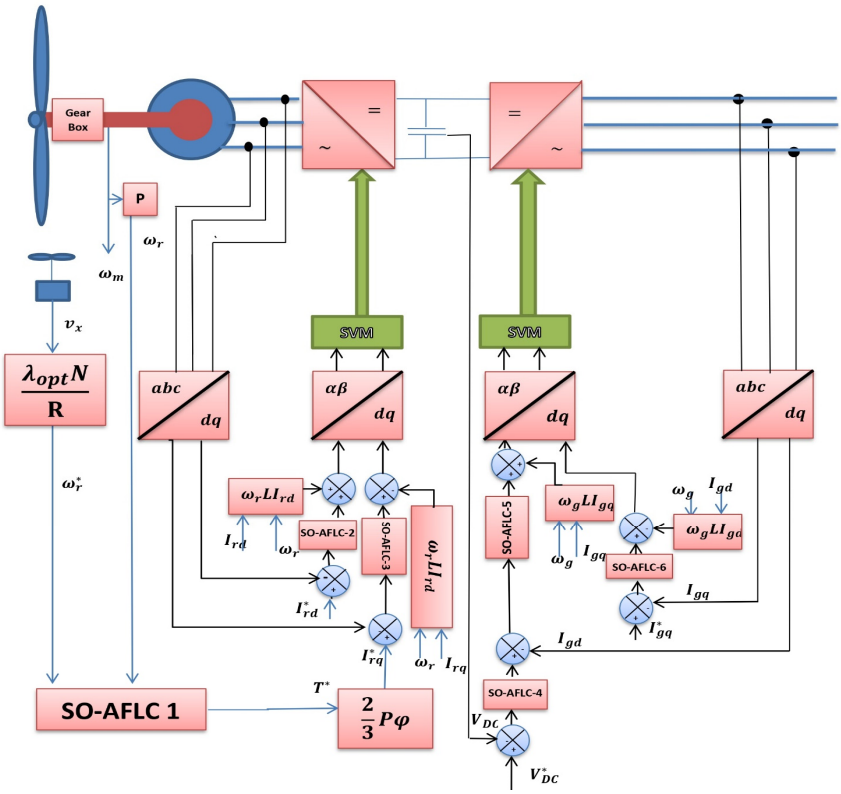



**Figure 2.** Schematic representation of the PMSG wind power plant.

The mechanical power captured by the wind turbine is governed by the aerodynamic characteristics of the rotor and can be expressed as [16,37]:

$$P_m = \frac{1}{2}\rho A {v_w}^3 C_p(\lambda, \beta) \tag{1}$$

The power extracted from the wind depends primarily on the power coefficient, ($C_p$), which is a nonlinear function of the tip speed ratio, ($\lambda$), and the blade pitch angle, ($\beta$). The tip speed ratio is defined as

$$\lambda = \frac{R\omega}{v_w} \tag{2}$$

The mathematical relationship describing the power coefficient is given by

$$C_p(\lambda, \beta) = G_1\left\{\frac{G_2}{\lambda_i} - G_3\beta - DG_4\right\}e^{\frac{G_5}{F}} + G_6\lambda \tag{3}$$

$$\frac{1}{F} = \frac{1}{0.08\beta + \lambda} - \frac{0.035}{1 + \beta^3} \tag{4}$$

where ($G_1$):($G_6$) denote the empirical coefficients that characterize the aerodynamic behavior of the selected wind turbine.

$$G_1 = 0.5176; G_2 = 116; G_3 = 0.4; G_4 = 5; G_5 = -21; G_6 = 0.0068;$$

Figure 3 shows the association between the tip speed ratio ($\lambda$) and the power coefficient ($C_p$) for different values of $\beta$. Maximum power extraction from the wind turbine is attained when $C_p$ reaches its highest value, corresponding to the optimal tip speed ratio ($\lambda_{opt}$). Under this operating condition, the turbine converts the available wind energy into mechanical power with the highest possible efficiency.

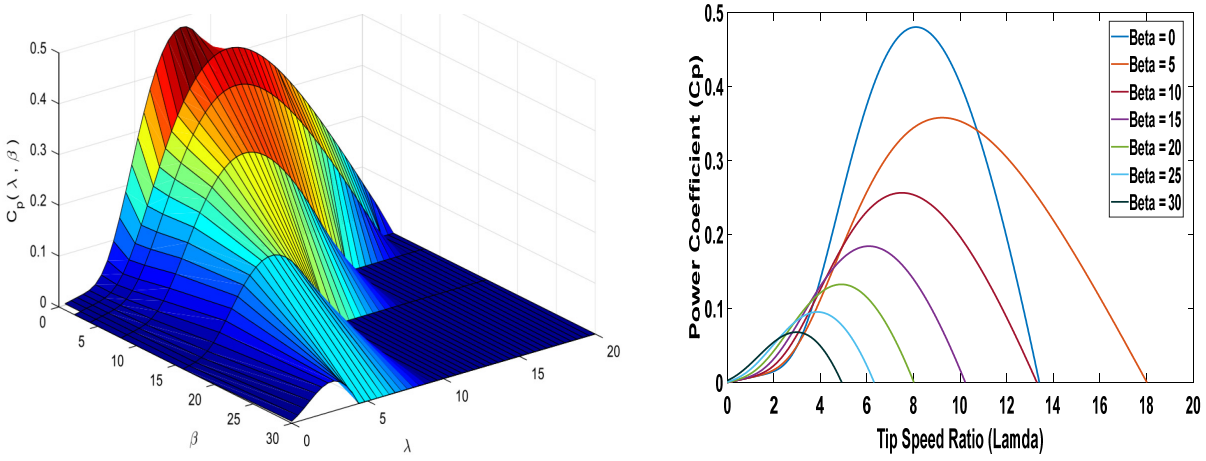



**Figure 3.** The features of wind turbines.

As indicated by the turbine parameters considered in this work, the optimum operating condition is obtained when the blade pitch angle is maintained at ($\beta = 0°$). Under this operating point, the optimal tip speed ratio is ($\lambda_{opt} = 8.1$), corresponding to a maximum power coefficient of approximately ($C_{p_{max}} = 0.48$), as illustrated in Figure 3. Therefore, the primary objective of the suggested control strategy is to continuously maintain the turbine operation around this optimal point despite variations in wind speed, thereby maximizing the extracted wind power and improving the overall efficiency of the energy conversion system.

### *2.1. Second-Order Adaptive Fuzzy Logic Controller*

The suggested control approach is based on a SO-AFLC, also referred to as a second-order adaptive sliding mode controller (SO-ASMC). This controller combines the adaptive capability of AFLC with the robustness of second-order sliding mode control (SO-SMC), enabling high tracking accuracy while maintaining excellent dynamic performance under rapidly changing operating conditions [35]. The overall configuration of the proposed controller is illustrated in Figure 4. The SO-AFLC consists of two complementary control components. The adaptive fuzzy logic controller is primarily responsible for steady-state operation, where it minimizes oscillations and reduces the chattering phenomenon commonly associated with conventional sliding mode control. During transient operating conditions or sudden disturbances, the second-order sliding mode controller becomes dominant, providing fast convergence, enhanced disturbance rejection, and improved robustness. By combining these two control mechanisms, the proposed controller achieves both smooth steady-state behavior and rapid transient response. The controller design begins with the definition of an appropriate sliding surface, which serves as the basis for the sliding mode control law. The objective of the sliding surface is to force the tracking error and its derivatives toward zero, thereby ensuring accurate reference tracking and stable closed-loop operation [35–41]. In the proposed design, the sliding surface is formulated using the second derivative of the tracking error together with the adaptive fuzzy control output and is expressed as

$$SS = K_L \ddot{e}(t) + \zeta(t) \tag{5}$$

where the AFLC's output is represented by $\zeta(t)$, $K_L$ weights the second-order error dynamics, and $e(t)$ is the tracking error or the deviation between the desired value and the measured controlled variable. The use of the second derivative is not obtained through an ideal direct differentiation of a noisy measured signal. In the real-time implementation, the derivative-related quantities are obtained from sampled tracking-error data using appropriate numerical filtering/derivative processing before being supplied to the controller. This treatment is necessary to avoid excessive amplification of measurement noise and numerical noise. The control output is generated from the sliding variable using a continuous saturation approximation of the switching action. To suppress undesirable switching oscillations and alleviate the chattering effect introduced by pulse-width modulation (PWM), a continuous saturation function is incorporated into the control law. Accordingly, the desired controller output is determined by

$$Desired\ Output = -\Lambda\ \mathrm{sat}(\mathrm{SS}, \rho) = -\Lambda \left[ \frac{SS}{|SS| + \varrho} \right] \tag{6}$$

where $\varrho > 0$, $\varrho \approx 0$ defines the boundary-layer thickness and $\Lambda > 0$ is the sliding-control gain. A smaller $\rho$ gives a closer approximation to the ideal sliding condition but can increase sensitivity to measurement noise and numerical effects; a larger $\varrho$ reduces switching activity at the expense of a larger residual tracking band. $\Lambda$ is selected sufficiently large to dominate the bounded lumped uncertainty in the sliding-variable dynamics while avoiding unnecessarily aggressive control action.

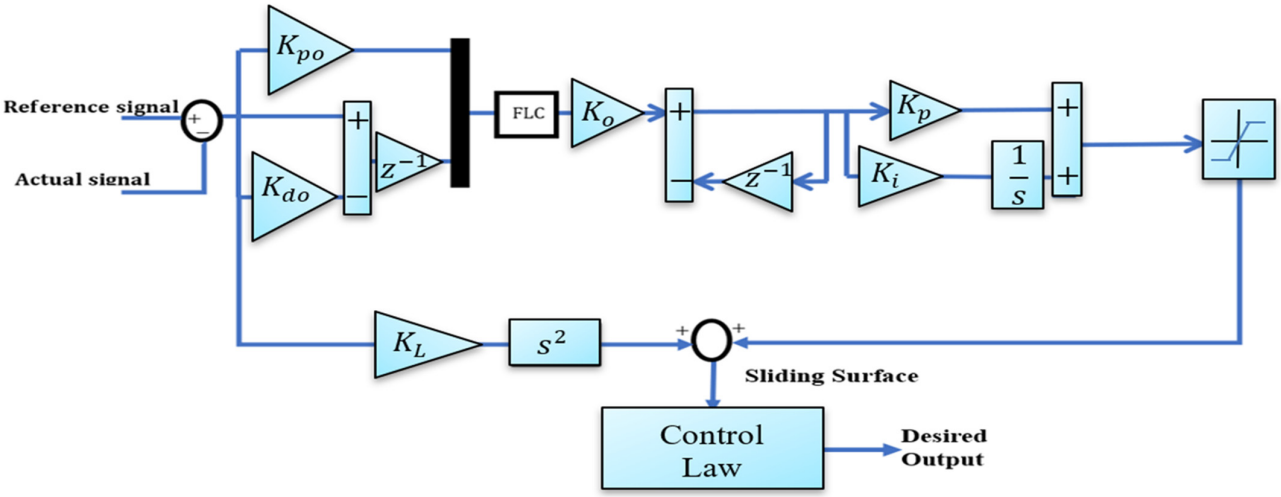



**Figure 4.** Architecture of a SO-AFLC scheme.

The fuzzy inference system employed in the proposed SO-AFLC is depicted in Figure 5. The fuzzy inference system uses seven linguistic variables for both inputs ($e$ and $\Delta e$) Negative Small (NS), Zero (Z), Negative Big (NB), Negative Medium (NM), Positive Medium (PM), Positive Small (PS), and Positive Big (PB). The approximate input breakpoints shown in Figure 5a are: NB = (−2,−1,−0.67), NM = (−1,−0.67,−0.3), NS = (−0.67,−0.33,0), Z = (−0.33,0,0.33), PS = (0,0.33,0.67), PM = (0.33,0.67,1), and PB = (0.67,1,2). But the output variables are represented using nine linguistic variables: Negative Small (NS), Zero (Z), Negative Big (NB), Negative Medium (NM), Positive Medium (PM), Positive Small (PS), Negative very small (NVS), Positive very small (PVS) and Positive Big (PB). The approximate output centers/breakpoints shown in Figure 5b are NB shoulder, NM = −0.75, NS = −0.50, NVS = −0.25, Z = 0, PVS = 0.25, PS = 0.50, PM = 0.75, and PB shoulder. To describe these linguistic variables, overlapping triangular membership functions are selected because they offer a favorable compromise between computational efficiency, implementation simplicity, and control accuracy. Their widespread adoption in fuzzy control applications has demonstrated reliable performance while maintaining a relatively low computational burden [15–17,37]. The controller decision-making process is governed by a Mamdani-type fuzzy inference mechanism consisting of 49 control rules, summarized in Table 1. These rules establish the relationship between the tracking error, its alteration rate, and the corresponding control measure. The rule base was carefully designed to balance response speed, robustness, and computational complexity. Consequently, the proposed adaptive fuzzy controller provides accurate reference tracking, improved disturbance rejection, and enhanced dynamic behavior under a variety of operational circumstances. By integrating adaptive fuzzy reasoning with SO-SMC, the suggested SO-AFLC effectively exploits the advantages of both techniques. The fuzzy component continuously adjusts the controller behavior according to system operating conditions, whereas the sliding mode component guarantees rapid convergence and resilience against external perturbations and model uncertainties. As a result, the combined controller exhibits superior stability, reduced steady-state error, faster transient response, and improved overall control functionality compared with traditional PI and AFLC.

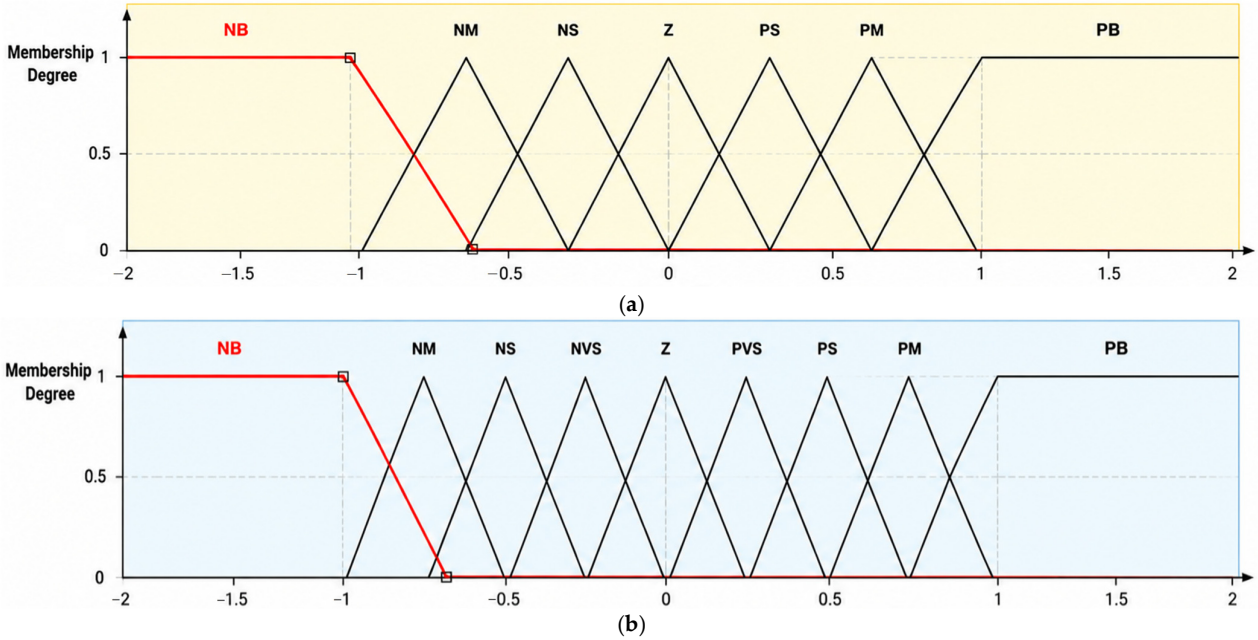



**Figure 5.** Membership Functions; (**a**) for inputs; and (**b**) output.

**Table 1.** AFLC rule base.

| e<br>Δe | NM | NS | PM | NB | PS | Z | PB |
|---|---|---|---|---|---|---|---|
| **NB** | NB | NB | NVS | NB | NS | NM | Z |
| **PS** | NVS | Z | PM | NS | PS | PVS | PB |
| **NS** | NM | NS | PVS | NB | Z | NVS | PS |
| **NM** | NB | NM | Z | NB | NVS | NS | PVS |
| **Z** | NS | NVS | PS | NM | PVS | Z | PM |
| **PB** | PVS | PS | PB | Z | PB | PM | PB |
| **PM** | Z | PVS | PB | NVS | PM | PS | PB |

### *2.2. Machine-Side Converter (MSC)*

The main objective of the MSC is to control the rotational speed of the permanent magnet synchronous generator (PMSG) so that the wind turbine continuously operates at the maximum power point despite variations in wind speed. The overall MSC control configuration is presented in Figure 6. For a variable-speed wind turbine, maximum energy extraction is achieved when the aerodynamic power coefficient, ($C_p$), reaches its peak value. Since ($C_p$) is governed by both the blade pitch angle ($\beta$) and the tip speed ratio ($\lambda$), maintaining the turbine at its optimal operating point requires continuous adjustment of the generator speed. As shown in Figure 3, the highest aerodynamic efficiency corresponds to ($C_{p_{max}} \approx 0.48$), which is attained when the pitch angle of the blade remains at zero and the tip speed ratio stays at its optimum value of ($\lambda_{opt} = 8.1$). Because speed varies continuously during operation, the reference rotor speed must be updated accordingly to preserve the optimum tip speed ratio ($\lambda_{opt}$). This enables the turbine to maximize the conversion of available wind energy into mechanical power while maintaining high operating efficiency over a broad range of wind conditions. To accomplish this objective, the MSC incorporates three coordinated control loops (Controllers 1–3), as illustrated in Figure 6. These controllers regulate the generator currents and electromagnetic torque, ensuring accurate rotor-speed tracking, rapid dynamic response, and effective maximum power point tracking under continuously changing wind conditions [6,42].

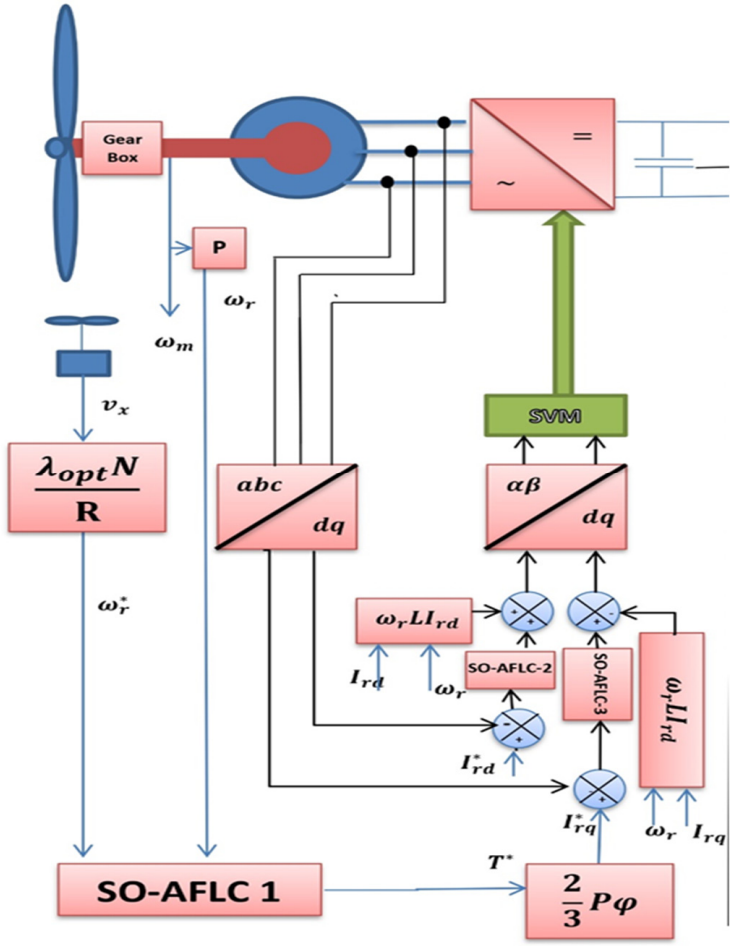



**Figure 6.** Machine Side Converter block diagram.

### *2.3. Grid-Connected Converter (GCC)*

The Grid-Connected Converter (GCC) provides the electrical interface between the back-to-back converter and the utility grid. Its control structure, illustrated in Figure 7, is designed to maintain stable power exchange while ensuring compliance with grid operating requirements. The principal responsibilities of the GCC are to regulate the DC-link voltage and control the reactive power exchanged with the utility network. Stable DC-link voltage regulation is essential for maintaining the power balance between the machine-side and Grid-Connected Converter, thereby ensuring reliable operation of the complete WECS. Simultaneously, reactive power control enables the converter to satisfy grid-code requirements and enhance the network's overall power delivery. These objectives are accomplished through three coordinated control loops (Controllers 4–6) integrated within the GCC control architecture. The DC link voltage controller maintains the capacitor voltage close to its constant reference value despite fluctuations in generated power, as illustrated in Equation (7).

$$C_{link}\frac{dV_{dc}}{dt} = I_{MSC} - I_{GSC} \tag{7}$$

where $C_{link}$ is the DC-link capacitance, while $I_{MSC}$ and $I_{GSC}$ denote the currents supplied by the machine-side and grid-side converters, respectively.

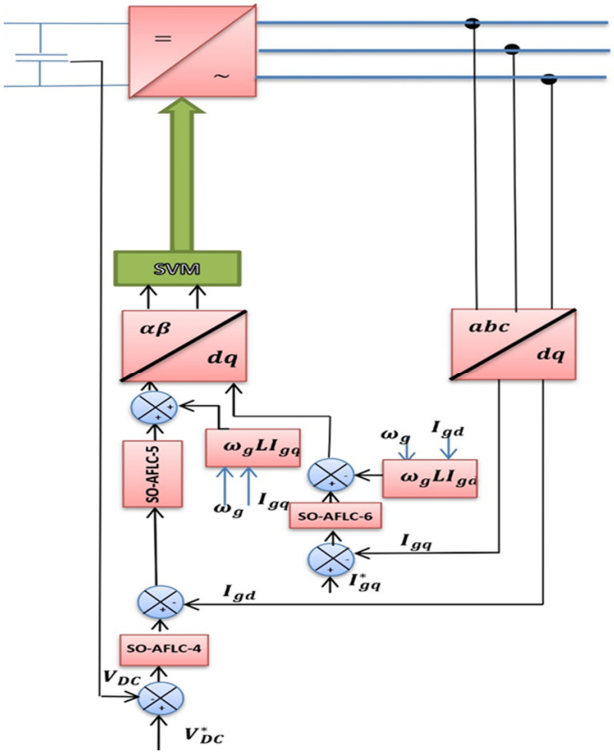



**Figure 7.** Grid-Connected Converter (GCC) block diagram.

In this study, the reference reactive power is selected as zero, allowing the wind energy conversion system to operate at unity power factor. This operating strategy minimizes unnecessary reactive power flow, enhances converter stability, improves voltage regulation, and increases compatibility with modern electrical grids [43,44].

The reactive power equation is:

$$Q_g = \frac{3}{2}\left(v_{gq} i_{gd} - v_{gd} i_{gq}\right) \tag{8}$$

Under grid-voltage-oriented control, the $d$-axis is aligned with the grid voltage vector, resulting in:

$$v_{gq} = 0 \tag{9}$$

Thus, (8) becomes:

$$Q_g = -\frac{3}{2} v_{gd} i_{gq} \tag{10}$$

To achieve unity power factor operation: $Q_g = 0$, which implies: $i_{gq} = 0$. Hence, the reactive current component is forced to zero, ensuring that the injected grid current remains in phase with the grid voltage, thereby achieving unity power factor operation and improving power quality.

### *2.4. Modelling of PMSG*

The dynamic behavior of the permanent magnet synchronous generator (PMSG) can be described in the rotating (dq) reference frame, as reported in [45,46]. The dq-axis transformation converts the three-phase stator quantities into two orthogonal components, namely the $v_{sd}$ and $v_{sq}$ components. This representation considerably simplifies the analysis and control of the PMSG because the resulting electrical variables can be directly related to the rotor position and electromagnetic torque.

$$v_{sd} = \omega_e L_q I_{sq} - R_s I_{sd} - L_d \frac{dI_{sd}}{dt} \tag{11}$$

$$v_{sq} = \omega_e \psi_m - R_s I_{sq} - L_q \frac{dI_{sq}}{dt} - \omega_e L_d I_{sd} \tag{12}$$

where $v_{sd}$ and $v_{sq}$ denote the stator voltage components along the d-q axes, respectively; $I_{sd}$ and $I_{sq}$ are the corresponding stator current components; $R_s$ is the stator winding resistance; $\omega_e$ is the electrical angular speed of the generator; $L_q$ and $L_d$ are the d-q axis inductance, and $\psi_m$ represent the permanent flux linkages.

The electromagnetic torque developed by the PMSG is given by [46] as

$$T_e = \frac{3}{2} p I_{sq} \left( L_d - L_q \right) I_{sd} \tag{13}$$

In a surface-mounted PMSG, $L_d = L_q = L_s$ and $p$ is the number of pole pairs. As a result, the electromagnetic torque given by (13) can be rewritten as:

$$T_e = \frac{3}{2} p I_{sq} \psi_m \tag{14}$$

## 3. Simulation Results

To assess the effectiveness of the proposed control strategy, a detailed model of the grid-connected PMSG-based wind energy conversion system was developed in MATLAB/Simulink R2026a. The machine and converter parameters adopted in the simulations are listed in Table 2, while the optimized controller settings are summarized in Table 3. All six controllers in both GCC and MSC are simultaneously replaced by the proposed method. The proportional and integral gains of the conventional PI regulators were optimized offline using the Marine Predators Algorithm (MPA) [9], with the Integral Absolute Error (IAE) adopted as the objective function. To ensure a consistent and fair comparison, the AFLC and SO-AFLC parameters were also tuned offline using MPA under the same optimization framework and tuning conditions. Consequently, all three topologies were evaluated using parameter sets obtained through a common IAE-based optimization procedure, while preserving the specific structure and parameters of each control strategy. The performance of the proposed SO-AFLC is investigated under two operating scenarios. The first considers abrupt step variations in wind speed to assess transient response and disturbance-rejection capability, whereas the second employs measured wind-speed data to evaluate controller performance under realistic operating conditions. In both scenarios, the SO-AFLC is compared with the conventionally optimized PI and AFLC controllers under identical operating conditions.

**Table 2.** Model specifications.

| Power | $P_{nom} = 10$ kw |
|---|---|
| Input Voltage | $V_{nom} = 575$ V |
| Input Frequency | f = 50 Hz |
| Stator Resistance | $R_s = 0.00829$ ohm |
| Stator Direct Inductance | $L_d = 0.174$ mH |
| Stator quadrature Inductance | $L_q = 0.174$ mH |
| Permanent magnet flux | $\varphi = 0.0707$ wb |
| No. of pole pairs | $P = 6$ |
| Inertia of the whole system | $J = 0.0875$ kg.m$^2$ |
| Friction Factor | $B = 0.0047$ N.m |

**Table 3.** Controller parameters.

| | | Controller 1 | Controller 2 | Controller 3 | Controller 4 | Controller 5 | Controller 6 |
|---|---|---|---|---|---|---|---|
| **PI** | $K_p$ | **8.12** | 5.67 | 7.45 | 4.98 | 1.25 | 3.89 |
| | $K_i$ | **3.76** | 2.14 | 4.02 | 1.83 | 3.56 | 1.47 |
| ***AFLC*** | $K_0$ | ***0.85*** | 1.94 | 0.42 | 1.12 | 1.67 | 2.21 |
| | $K_{po}$ | ***11.36*** | 6.42 | 2.05 | 7.58 | 0.91 | 9.14 |
| | $K_{do}$ | ***5.12*** | 2.03 | 3.44 | 0.67 | 6.28 | 0.34 |
| | $K_p$ | ***10.45*** | 6.78 | 7.92 | 2.31 | 0.45 | 5.89 |
| | $K_i$ | ***4.98*** | 1.96 | 0.84 | 0.73 | 5.62 | 0.15 |
| ***SO-AFLC*** | $K_0$ | ***2.94*** | 3.12 | 0.63 | 1.45 | 2.08 | 3.76 |
| | $K_{po}$ | ***13.52*** | 6.91 | 1.84 | 8.67 | 0.72 | 9.33 |
| | $K_{do}$ | ***6.85*** | 2.41 | 4.12 | 0.58 | 7.11 | 0.49 |
| | $K_p$ | ***11.73*** | 8.02 | 9.48 | 2.14 | 0.67 | 7.95 |
| | $K_i$ | ***5.84*** | 2.96 | 2.18 | 0.92 | 8.37 | 0.28 |
| | $K_L$ | ***3.12*** | 2.05 | 1.67 | 1.48 | 1.26 | 2.34 |

### *3.1. Case 1: Step Wind Speed Profile*

In this case, a step-wise wind speed profile is applied to evaluate the dynamic performance and robustness of the SO-AFLC under abrupt variations. The speed profile is illustrated in Figure 8. Figure 9 illustrates the dynamic response of the power coefficient under different control strategies. The SO-AFLC achieves the closest tracking to the optimal value (~0.48), with significantly reduced oscillations compared to both conventional PI and AFLC. During transient disturbances (zoomed regions), the PI controller exhibits pronounced fluctuations and slower damping, while AFLC improves stability but still shows minor deviations. In contrast, SO-AFLC demonstrates superior robustness, fast settling, and minimal steady-state error, ensuring efficient maximum power extraction under varying wind conditions. Figure 10 shows the evolution of the tip speed ratio. The SO-AFLC maintains λ tightly around its optimal reference, with faster convergence and reduced overshoot following disturbances. The PI controller exhibits pronounced voltage drops and a slower recovery response, highlighting its limited capability to adapt to dynamic operating conditions. Although the AFLC provides noticeable performance improvements, the SO-AFLC demonstrates the most effective control performance, offering enhanced transient response and superior damping characteristics. These improvements contribute to maintaining optimal aerodynamic operation throughout the disturbance period. Furthermore, the SO-AFLC achieves the smallest peak undershoot at (t = 3) s and exhibits reduced overshoot at (t = 1) s and (t = 2) s compared with the PI and AFLC controllers, confirming its robustness and effectiveness under varying operating conditions. Rotor speed responses obtained using the three controllers are illustrated in Figure 11. The conventional PI controller experiences relatively large oscillations accompanied by longer settling times after each disturbance. The AFLC improves the transient behavior by reducing oscillation amplitude; however, slight tracking deviations are still observed. In comparison, the SO-AFLC provides smooth speed transitions, excellent damping characteristics, and highly accurate reference tracking. The percentage of improvement is calculated based on error reduction as $I = (E_{baseline} - E_{SO-AFLC})/E_{baseline} \times 100$. Quantitatively, the proposed controller enhances rotor speed tracking by 53.26% relative to the PI regulator and 36.98% compared with the AFLC while simultaneously minimizing transient overshoot and undershoot. Figure 12 demonstrates the mechanical power response under successive step variations, where the conventional PI controller exhibits significant oscillations and noticeable steady-state ripple, indicating poor damping and limited adaptability to system

nonlinearities. The AFLC approach improves the response by reducing oscillation amplitude and enhancing transient behavior; however, residual fluctuations persist. In contrast, the proposed SO-AFLC achieves superior performance characterized by near-critically damped dynamics, negligible overshoot, and minimal steady-state variance, resulting in a smoother power profile and improved energy capture stability under dynamic operating conditions. The AFLC and SO-AFLC attained the lowest undershoot values in relation to the PI at t = 3 s. Figure 13 presents the control of DC voltage performance, where the traditional PI regulator shows considerable over/undershoot and sustained oscillations during disturbances, reflecting weak disturbance rejection capability. The AFLC method mitigates these effects to some extent by improving damping and reducing voltage excursions, yet transient deviations remain evident. The proposed SO-AFLC provides the most effective regulation, maintaining the DC-link voltage within a narrow tolerance band with fast settling, minimal ripple, and near-zero steady-state error, ensuring proper power balance and enhanced converter stability. Finally, Figure 14 presents the reactive power responses of the investigated control strategies while maintaining the reference reactive power at ($Q_{ref} = 0$) Var. The results demonstrate that the SO-AFLC outperforms both the conventional PI and AFLC controllers, exhibiting lower overshoot, reduced undershoot, and enhanced damping characteristics. In contrast, the SO-AFLC achieves highly stable reactive power control with rapid transient response, strong oscillation suppression, and negligible steady-state error, thereby ensuring smooth reactive power injection and improved compliance with grid voltage support requirements.

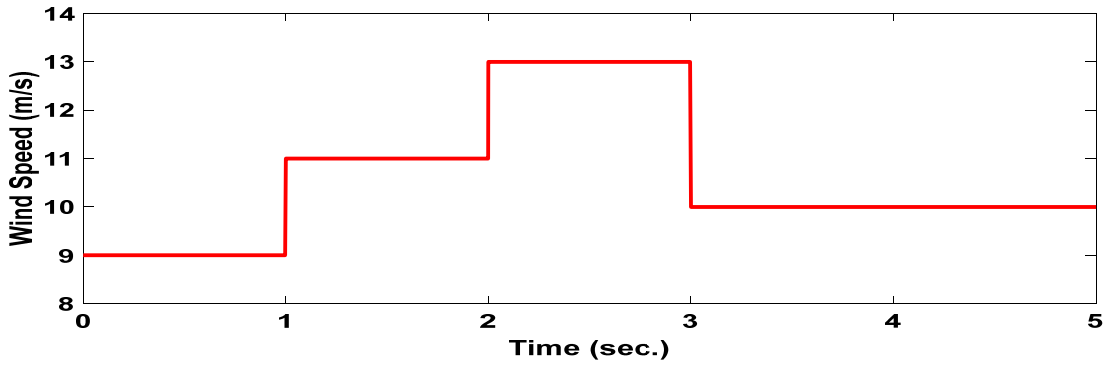



**Figure 8.** Wind speed variation profile.

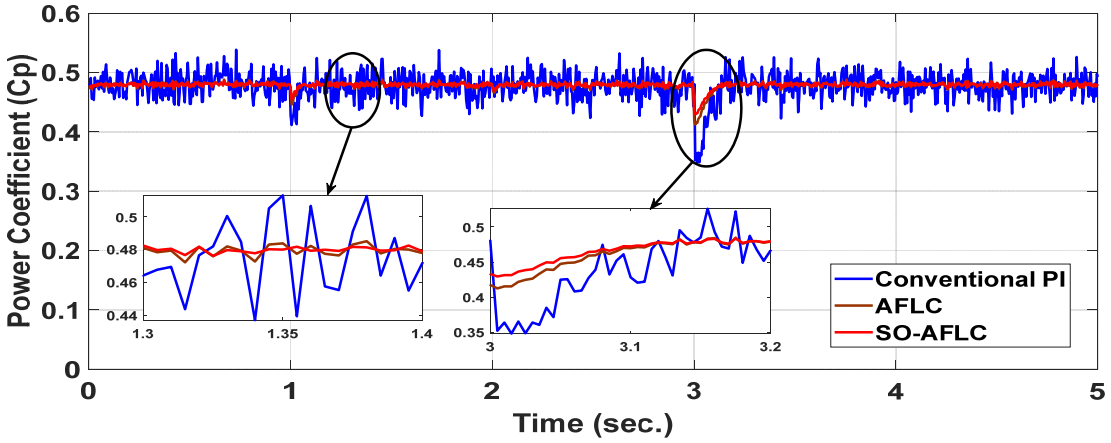



**Figure 9.** Evolution of Power coefficient ($C_p$) response.

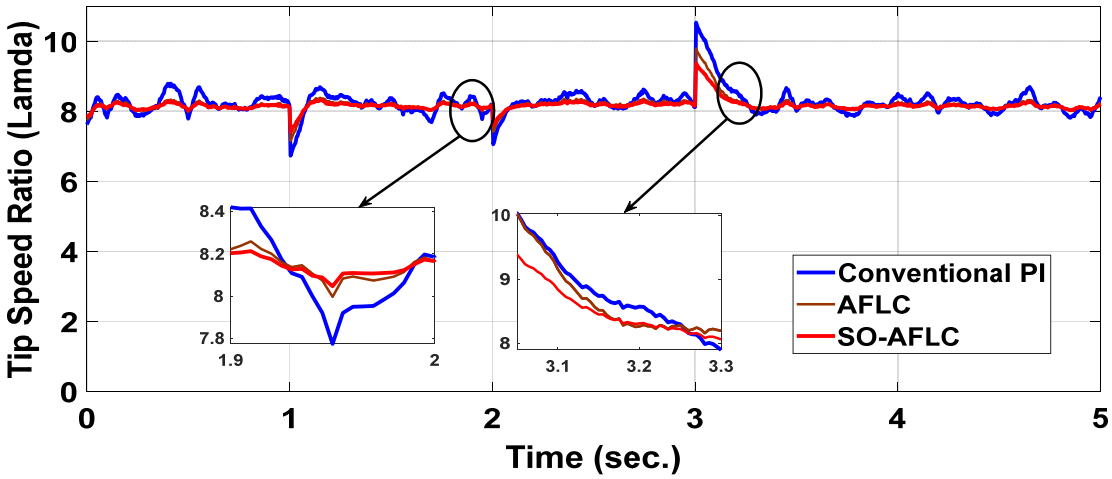



**Figure 10.** Evolution of the tip speed ratio.

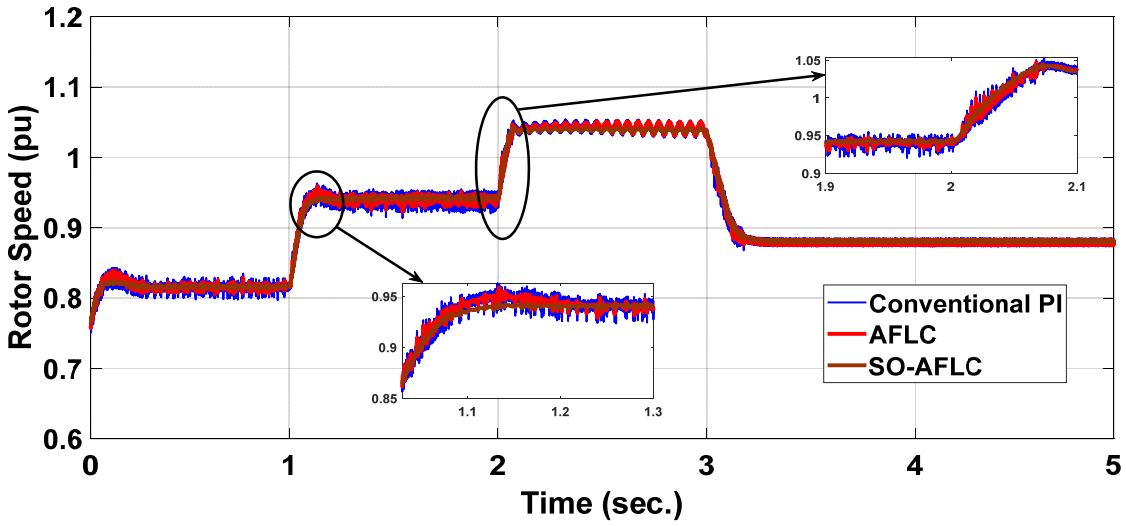



**Figure 11.** Evolution of Rotor Speed.

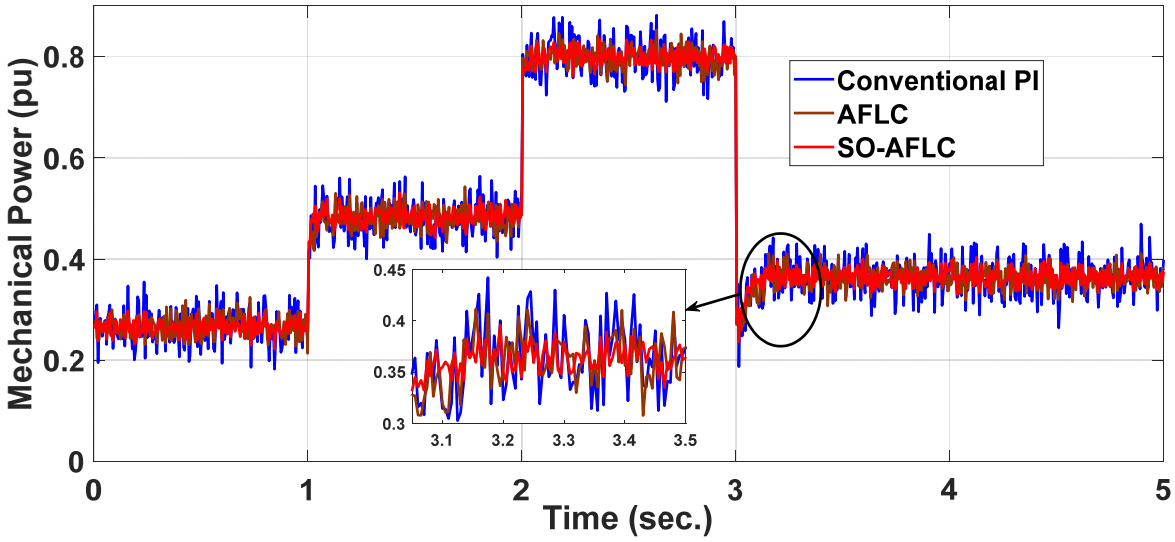



**Figure 12.** Evolution of Mechanical Power in (pu).

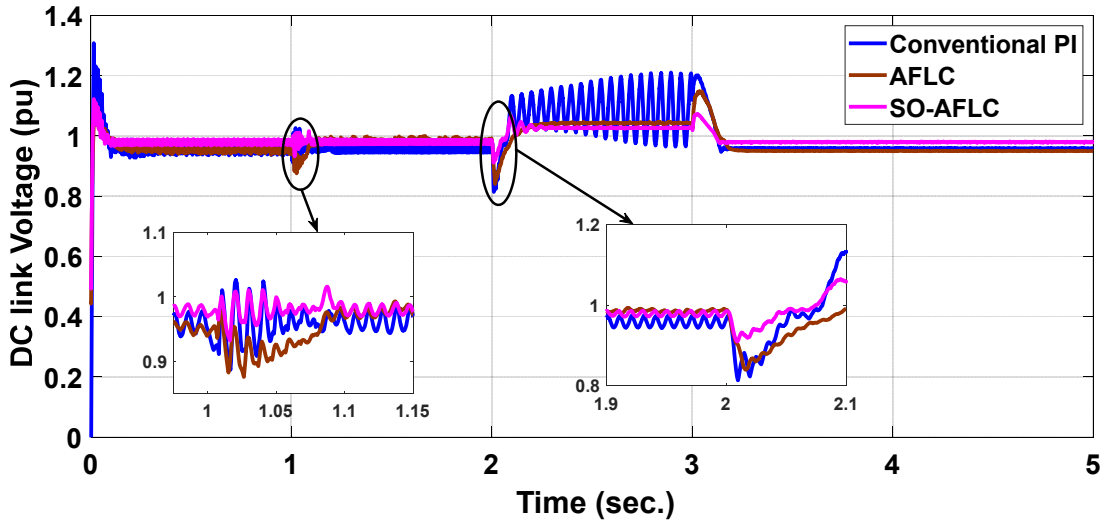



**Figure 13.** Evolution of DC link voltage.

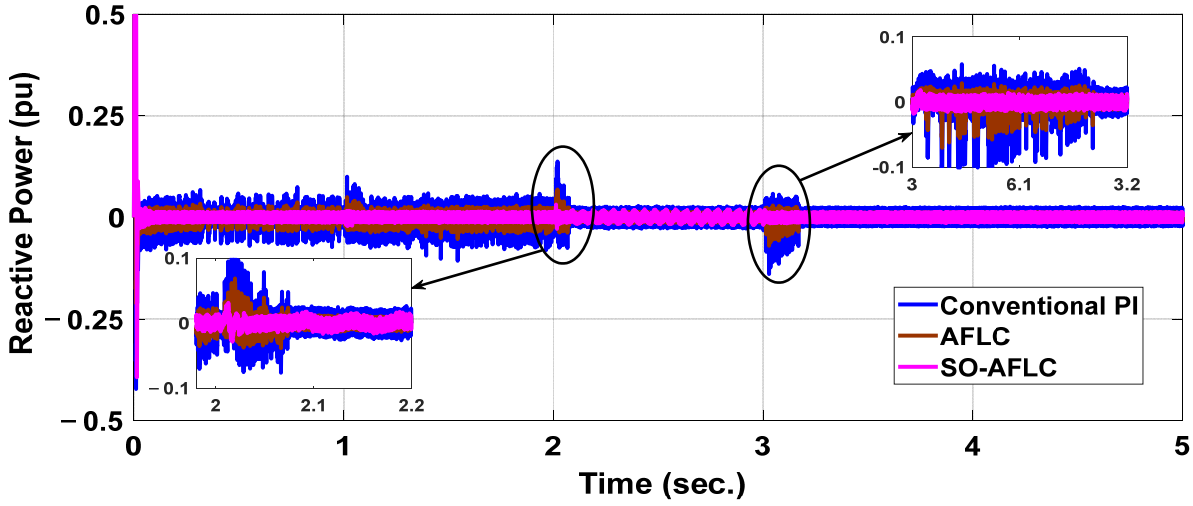



**Figure 14.** Reactive power delivered by the PMSG.

To provide a quantitative comparison of controller performance, the Integral Absolute Error (IAE) is employed as the primary performance index and is calculated using (15).

$$IAE = \int_0^{\infty} |e(t)| dt \tag{15}$$

Table 4 presents the IAE values for the six coordinated control loops. The mean IAE is 0.649817 for PI, 0.562483 for AFLC, and 0.511033 for SO-AFLC. The percentage reduction is calculated as $R = (IAE_{baseline} - IAE_{SO-AFLC})/IAE_{baseline} \times 100$. Accordingly, the SO-AFLC reduces the mean IAE by 21.36% relative to PI and 9.15% relative to AFLC.

**Table 4.** Comparative analysis of IAE for different control strategies.

| | Controller 1 | Controller 2 | Controller 3 | Controller 4 | Controller 5 | Controller 6 | Mean |
|---|---|---|---|---|---|---|---|
| **PI** | 0.12 | 1.238 | 0.6879 | 0.8932 | 0.2362 | 0.7236 | 0.649817 |
| **AFLC** | 0.08 | 1.0259 | 0.6223 | 0.7321 | 0.2125 | 0.7021 | 0.562483 |
| **SO-AFLC** | 0.0786 | 0.8698 | 0.5234 | 0.7021 | 0.2002 | 0.6921 | 0.511033 |

### *3.2. Case 2: Realistic Wind Speed Profile*

In this case, a realistic and time-varying wind speed profile is applied to emulate actual environmental operating conditions, characterized by continuous fluctuations and stochastic behavior. The wind data is derived from Ras Gharib, located along the Gulf of Suez, where the average monthly wind speed varies between 15 m/s in August and 7.5 m/s in January [47]. The measured wind profile, originally recorded over a duration of 480 min with a sampling frequency of $f_{actual} = 2$ Hz, is depicted in Figure 15. To ensure compatibility with the simulation and experimental time scales, the measured dataset was time-scaled and reprocessed over a 100-s interval. Specifically, the original time coordinate ($t_{data}$) was mapped to the new time coordinate ($t_{simulation}$) according to $t_{simulation} = \frac{100}{28,800} t_{data}$. Figure 16 presents the resulting time-scaled wind-speed profile used in the analysis. This time compression was adopted to provide a realistic yet computationally practical disturbance profile for evaluating the transient tracking of the investigated controllers. Importantly, the compression was applied exclusively to the time axis, without modifying the wind-speed amplitude. Consequently, the wind-speed operating range of the processed profile remains consistent with that of the original measured dataset. The power coefficient ($C_p$) behavior under the three control strategies is presented in Figure 17, where it is regulated around the optimal value of 0.48. Both SO-AFLC and AFLC outperform the typical PI controller, with SO-AFLC showing higher performance. Notably, the SO-AFLC outperforms the other approaches in terms of dip in range between $t = 40$ and $t = 45$ s. Furthermore, it decreases the steady-state inaccuracy in the $C_p$ response by 11.26% in comparison to AFLC and 58.23% in comparison to PI. Figure 18 shows the tip speed ratio ($\lambda$), which is optimized at 8.1 for all controllers. The steady-state accuracy of SO-AFLC is higher than that of AFLC and PI. During the transitory period between $t = 5$ s and $t = 15$ s, The level of overreach was decreased for both SO-AFLC and AFLC, with SO-AFLC doing somewhat better. Figure 19 depicts the PMSG's rotor speed response, in which both AFLC and SO-AFLC surpass the PI controller in tracking accuracy. The SO-AFLC distinguishes itself by offering a quicker dynamical reaction response. In terms of quantitative performance, it improves rotational speed tracking by 56.22% over PI and by 10.36% over AFLC. Figure 20 depicts the DC connection voltage between the MSC and GCC. The GCC keeps the DC voltage at a consistent reference level. In situations with strong winds, both SO-AFLC and AFLC reduce overreach, with SO-AFLC outperforming the former slightly. Furthermore, SO-AFLC has the minimum stabilization error of any controller. Figure 21 presents the reactive power responses of the investigated control strategies while maintaining the reference reactive power at ($Q_{ref} = 0$ Var). The results indicate that the proposed SO-AFLC provides superior reactive power regulation compared with the conventional PI and AFLC controllers, characterized by lower overshoot and undershoot, faster transient recovery, and improved damping. The SO-AFLC achieves a stable and well-damped reactive power response with rapid convergence and negligible steady-state error, demonstrating its effectiveness in suppressing oscillations and maintaining accurate reactive power tracking. These characteristics contribute to smoother reactive power regulation and improved dynamic support of the grid voltage.

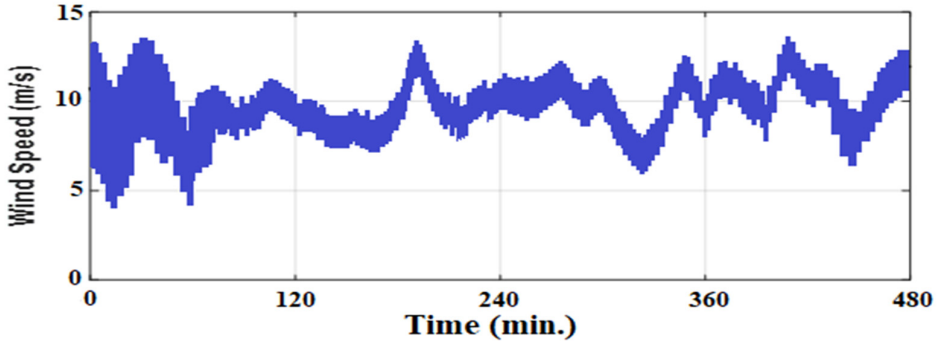



**Figure 15.** Actual measured wind speed profile.

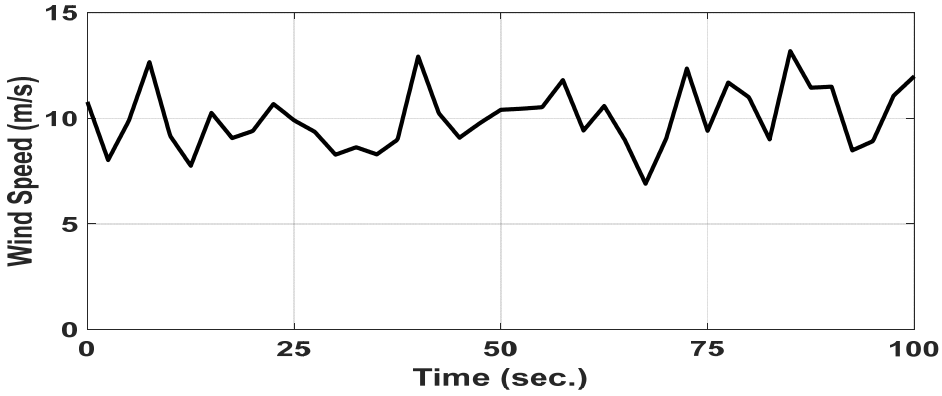



**Figure 16.** Estimated Wind speed curve.

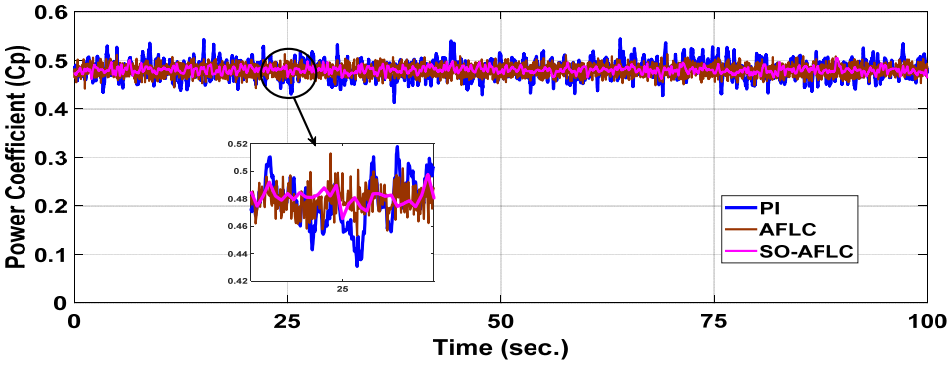



**Figure 17.** Evolution of Power coefficient.

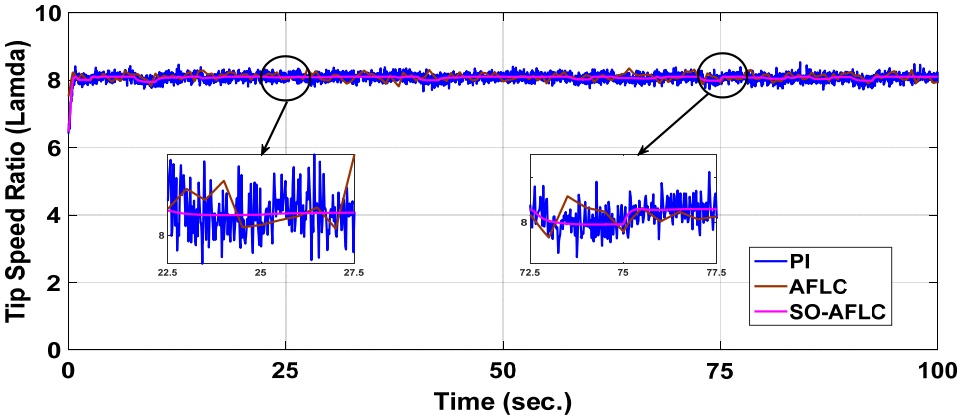



**Figure 18.** Evolution of Tip Speed Ratio.

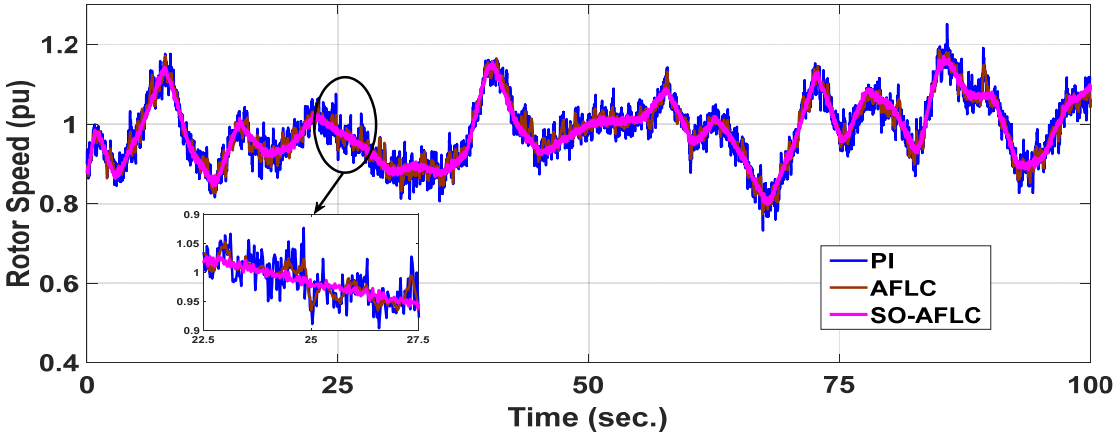



**Figure 19.** Evolution of Mechanical Rotor Speed.

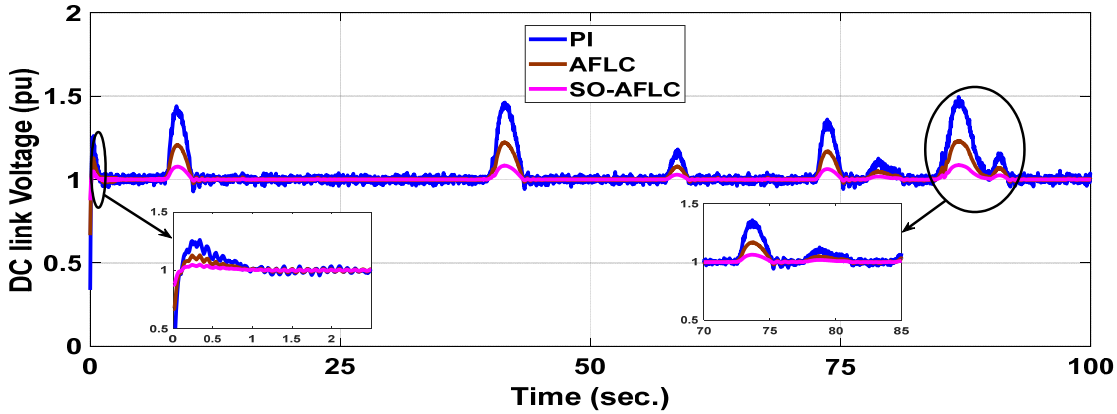



**Figure 20.** Evolution of DC link Voltage between GCC and MSC.

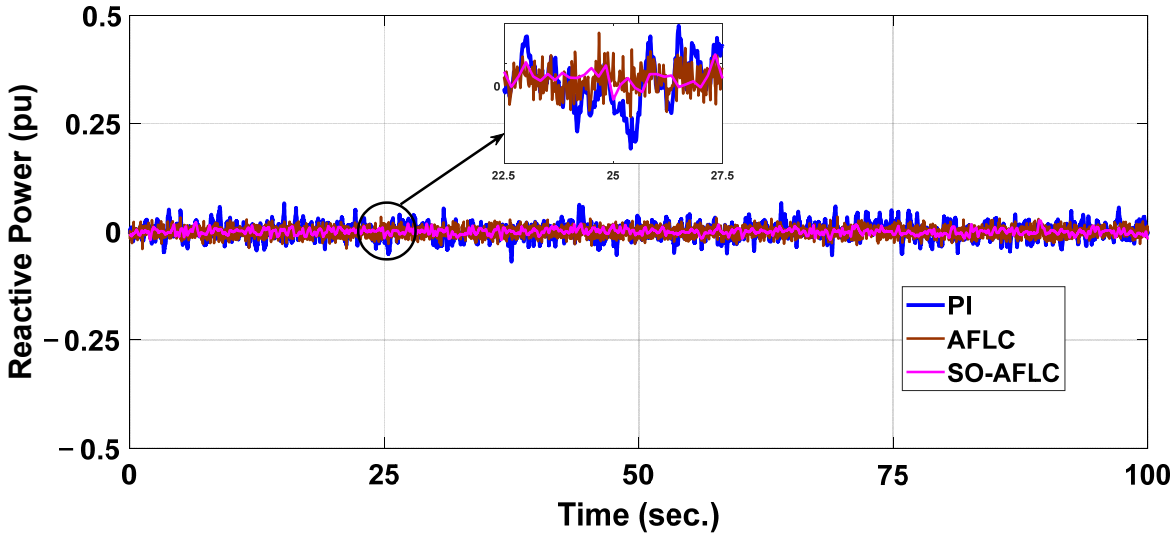



**Figure 21.** Evolution of Grid reactive power.

## 4. Experimental Setup

Figure 22 illustrates the configuration of the developed laboratory-scale experimental platform. In the proposed setup, a DC motor is utilized to emulate variable wind speed conditions and serves as the prime mover mechanically coupled to the permanent magnet synchronous generator (PMSG). The hardware parameters are illustrated in Table 5. The experimental system consists of several key components, including an incremental encoder

for rotor position and speed measurements, providing 1024 pulses per revolution and supporting rotational speeds of up to 6000 rpm, with a moment of inertia of 35 g·cm$^2$. The generation unit is a 2-pole PMSG rated at 0.2 kW, with nominal voltage ratings of 240/415 V at 50 Hz and a power factor of 1/0.75. In addition, the prime mover is a 250 W separately excited DC motor operating at a rated speed of 3000 rpm and supplied by a nominal voltage range of 180–220 VDC. The DC motor is mechanically coupled to the PMSG and is controlled to reproduce the rotor-speed conditions corresponding to the imposed wind-speed profile. The encoder provides the real-time rotor position and speed feedback required by the controller. This experimental arrangement enables real-time validation of the proposed control strategy under conditions that closely resemble practical operating scenarios. In the real-time implementation, the derivative terms required by the SO-AFLC are not obtained by directly differentiating the noisy measured rotor-speed signal, since such an operation can significantly amplify measurement noise and introduce undesirable high-frequency components into the control action. Instead, the tracking error is evaluated at each controller at sampling time. A digital filtering/derivative-processing procedure is applied between the sampled error signal and the SO-AFLC inputs to attenuate high-frequency measurement noise before the derivative quantities are used in the sliding-variable calculation. Consequently, the second-order information required by the controller is generated entirely from consecutive sampled error values and processed numerical derivative estimates, rather than from an ideal continuous-time differentiation of the measured signal. This procedure provides a practical compromise between derivative accuracy and noise attenuation and enables the SO-AFLC to be implemented reliably on the real-time control platform.

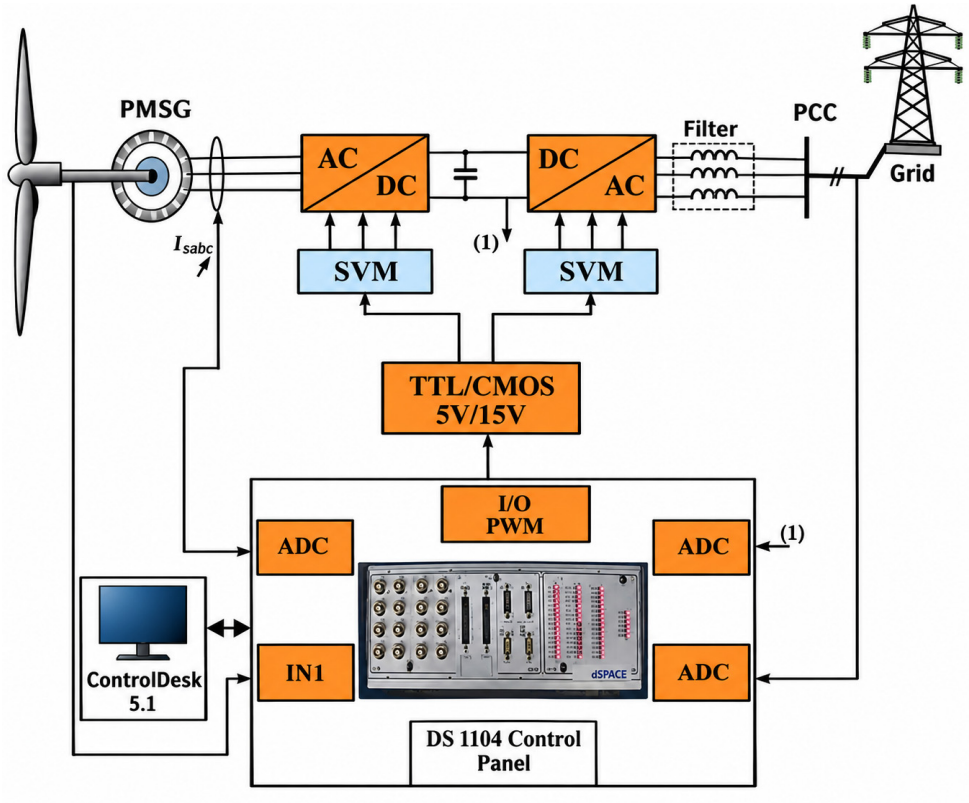



**Figure 22.** Real-time experimental platform for system verification.

**Table 5.** Hardware Parameters.

| Component | Specification |
| --- | --- |
| PMSG | The generation unit is a 2-pole rated at 0.2 kW, with nominal voltage ratings of 240/415 V at 50 Hz and a power factor of 1/0.75. |
| The prime mover | a 250 W separately excited DC motor operating at a rated speed of 3000 rpm and supplied by a nominal voltage range of 180–220 VDC |
| Position and speed sensor | Incremental encoder Speed: 6000 rpm, 1024 pulses, Moment of inertia: 35 g $cm^2$ |
| DC link Capacitor | 1000 µF |
| Grid Filter inductance | 2 mH |
| Grid Filter resistance | 0.1 Ω |
| Grid Voltage | 380 V |
| Grid frequency | 50 Hz |
| three-phase voltage-source inverter | the Mitsubishi CM50DY-24H |
| Current Sensor | LA-25NP |
| Voltage Sensor | LV25-P |
| Controller | dSPACE DS1104 |
| Software | MATLAB/Simulink 2026a + ControlDesk5.1 |
| PWM Frequency | 5 kHz |
| Sampling Frequency | 20 kHz |

## 5. Experimental Results

Figure 23 depicts the experimental validation of the PMSG-based WECS with the DS1104 real-time dSPACE control platform. In the developed system, a variable-speed direct current motor is intrinsically linked to the PMSG and serves as the prime mover to simulate variable wind speeds. By varying the motor speed, it emulates the changing wind speed conditions experienced by the generator. A rotary incremental encoder is attached to the generator shaft and provides digital feedback signals to the real-time control kit, allowing accurate actual feedback of rotor position and rotational speed. This configuration facilitates the implementation and verification of the suggested control method under operational circumstances. while ensuring reliable data acquisition and system monitoring.

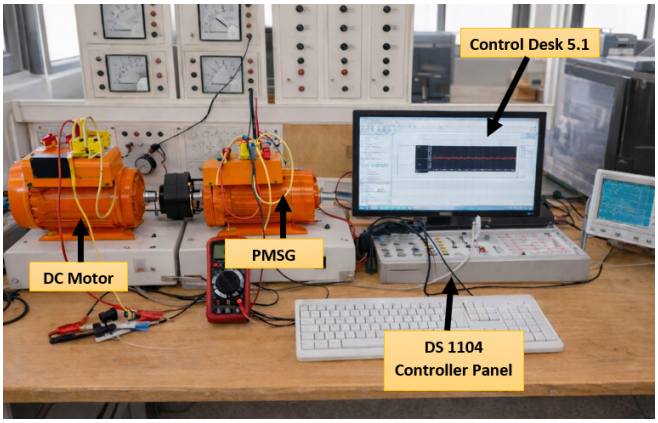



**Figure 23.** Wiring layout of the laboratory-scale experimental setup.

The laboratory hardware configuration of the PMSG-based WECS, implemented using the dSPACE DS1104 control board, is illustrated in Figure 23. The complete wiring arrangement of the experimental platform is also presented, highlighting the interconnection between the system components and the control hardware. The graphical user interface of the control system is developed using the DS1104 Real-Time Interface (RTI)

within ControlDesk 5.1, enabling real-time monitoring, data acquisition, and analysis of the experimental results. To evaluate the controller performance under varying operating conditions, the wind speed was emulated using a DC motor and varied in a stepwise manner, and in realistic data collected from Ras Gareb, Egypt.

### *5.1. Case I: Abrupt Step Wind Speed Profile*

In Case I, to evaluate the controller performance under varying operating conditions, the wind speed was emulated using a DC motor and varied in a stepwise manner at t = 1 s, 2 s, and 3 s, with values ranging from 9 m/s to 13 m/s, as illustrated in Figure 24. This experimental scenario was designed to replicate realistic wind fluctuations and assess the dynamic response and robustness of the proposed control strategy.

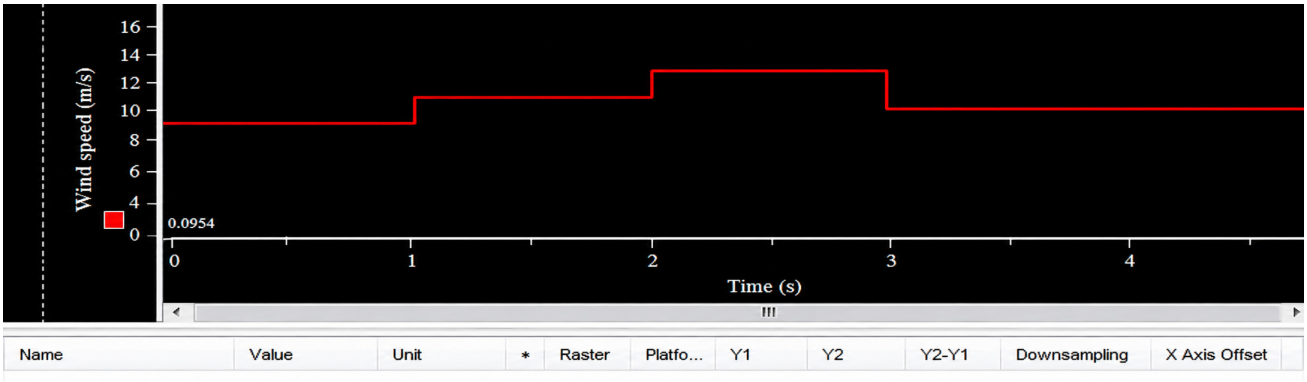
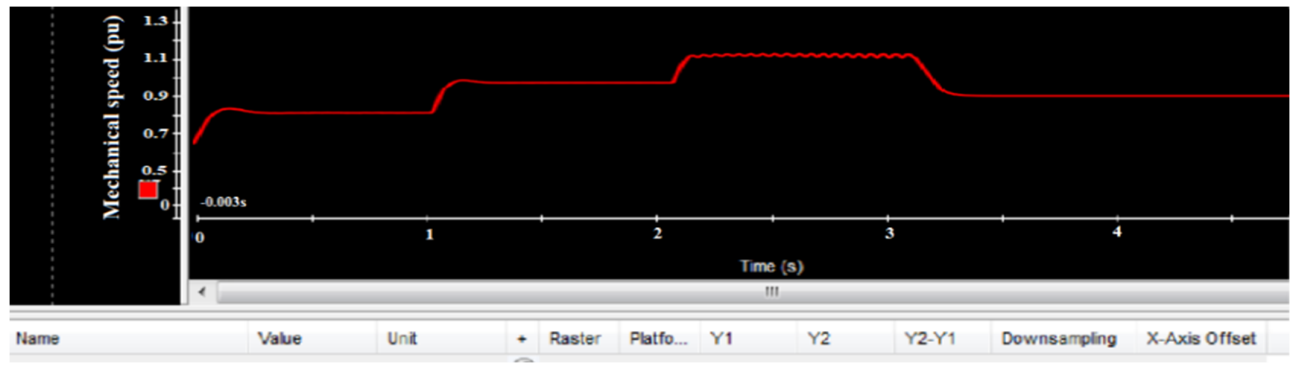



**Figure 24.** Real-time laboratory wind speed profile.

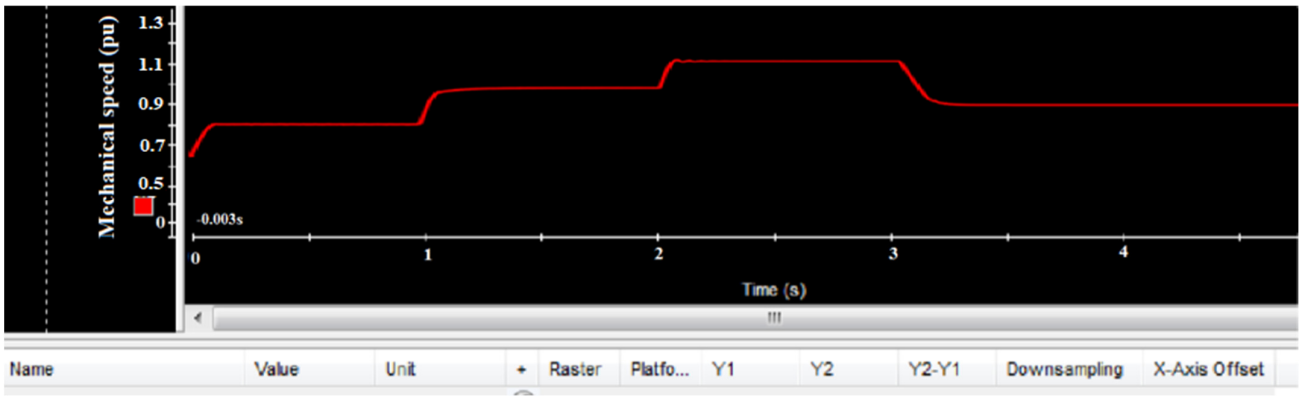
Figure 25 displays the rotor's mechanical speed response to wind speed fluctuations. The findings show that the proposed SO-AFLC has better dynamic performance than traditional PI and AFLC controllers. Specifically, the SO-AFLC allows the rotor speed to track its reference value more quickly after wind speed changes at t = 1 s, t = 2 s, and t = 3 s. Furthermore, it has better tracking precision. These data show that the SO-AFLC is successful at sustaining optimal rotor speed operating in a variety of wind situations. At t = 0 s, the proposed SO-AFLC achieved the lowest peak overshoot of 0.81 pu, compared with 0.85 pu for AFLC and 0.882 pu for PI, demonstrating its superior transient regulation capability. Quantitatively, the proposed controller improves rotor-speed tracking performance by 52.65% relative to PI and by 8.29% relative to AFLC.

Figure 26a–c confirm the effectiveness of the proposed controller in preserving the optimal power coefficient (Cp = 0.48) across varying wind speed scenarios. Compared with the PI and AFLC controllers, the SO-AFLC achieves an extremely rapid tracking response and improved adaptation to wind speed fluctuations occurring at t = 1 s, t = 2 s, and t = 3 s, thereby enhancing maximum power extraction capability. At t = 3 s, the proposed SO-AFLC exhibited the smallest deviation of the power coefficient Cp from its reference value of 0.48, with Cp reaching 0.43, compared with 0.41 for AFLC and 0.36 for PI. This result demonstrates the superior transient regulation capability of the proposed SO-AFLC.

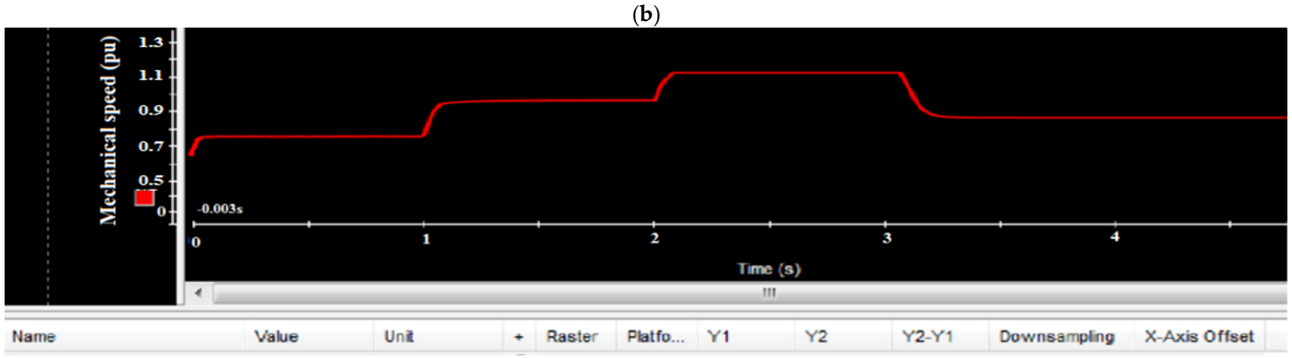
Figure 27a–c verify the capability of the proposed SO-AFLC to maintain the optimum tip speed ratio ($\lambda = 8.1$) under severe wind speed variations introduced at t = 1 s, t = 2 s, and t = 3 s. While both the AFLC and SO-AFLC outperform the traditional PI regulator in terms of response speed, the SO-AFLC delivers the highest control accuracy, ensuring precise reference tracking with minimal peak overshoot and negligible steady-state error. These findings demonstrate the benefit of the suggested controller in sustaining optimal turbine operation and maximizing energy capture under dynamic wind conditions.




(**a**)

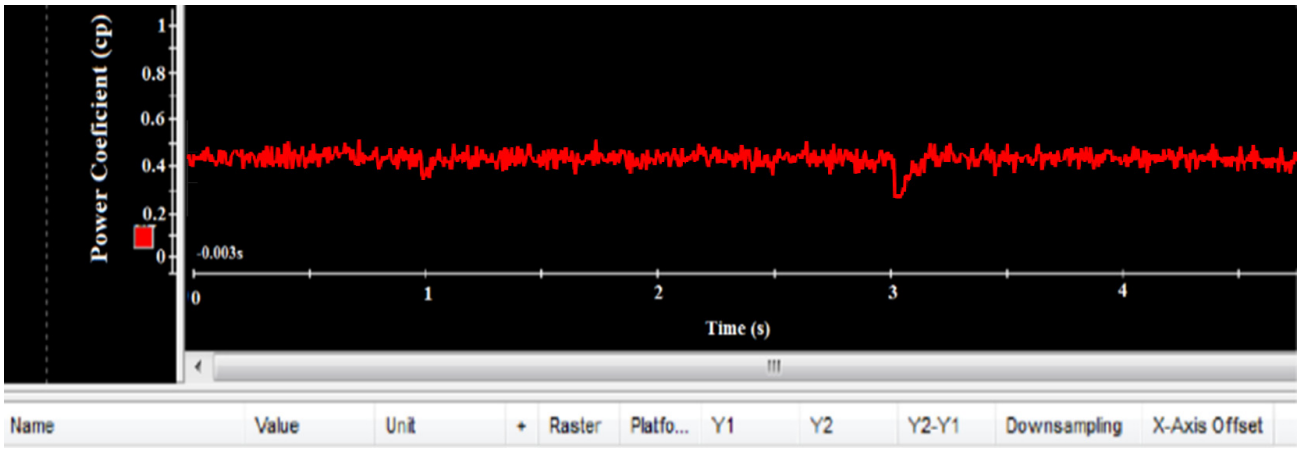



(**b**)



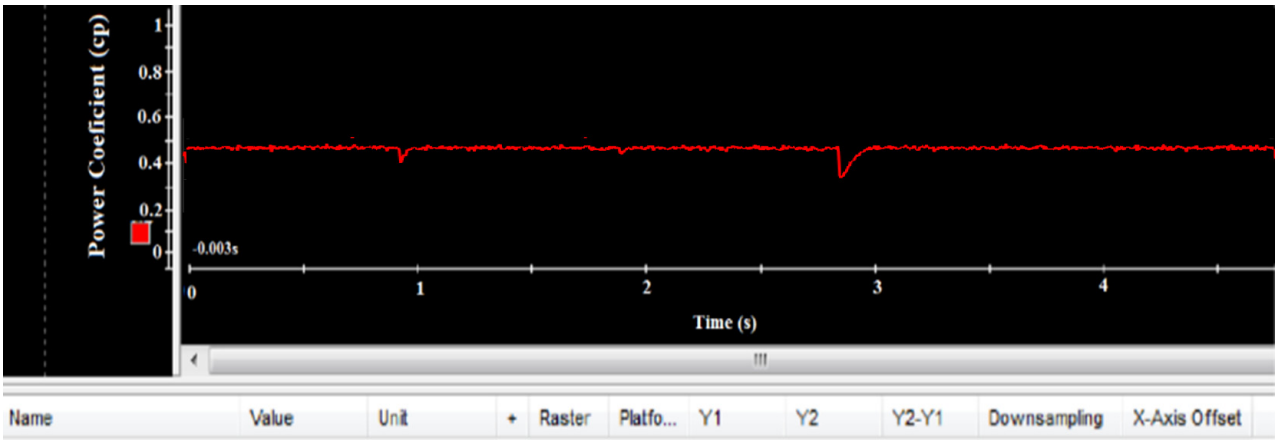

(**c**)

**Figure 25.** Real-time laboratory measured rotational speed using (**a**) PI controller, (**b**) AFLC, and (**c**) SO-AFLC.

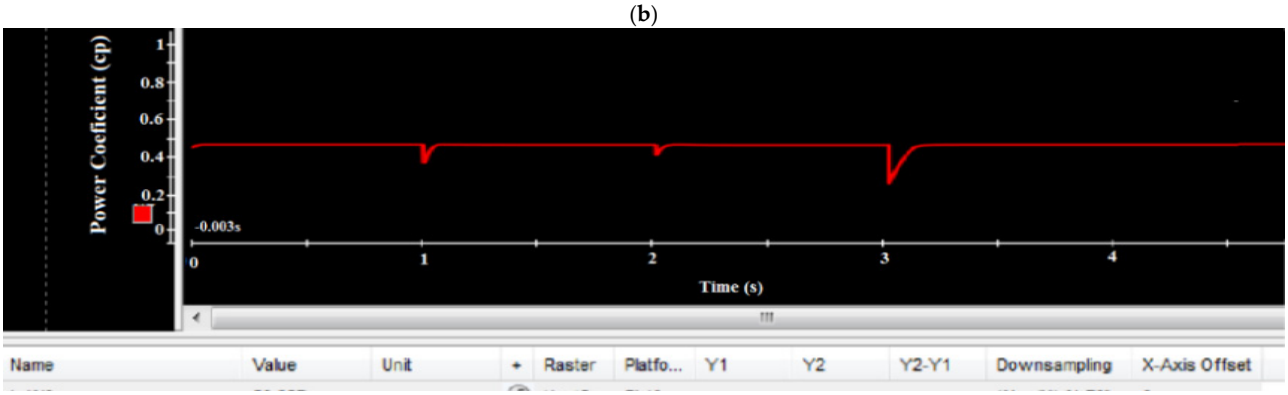



(**a**)

**Figure 26.** *Cont.*



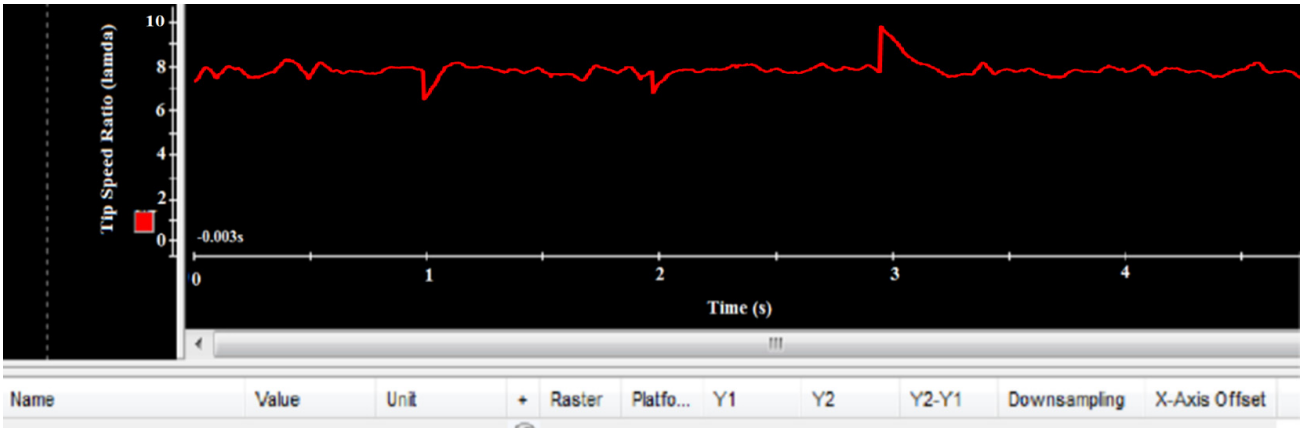

(**b**)




(**c**)

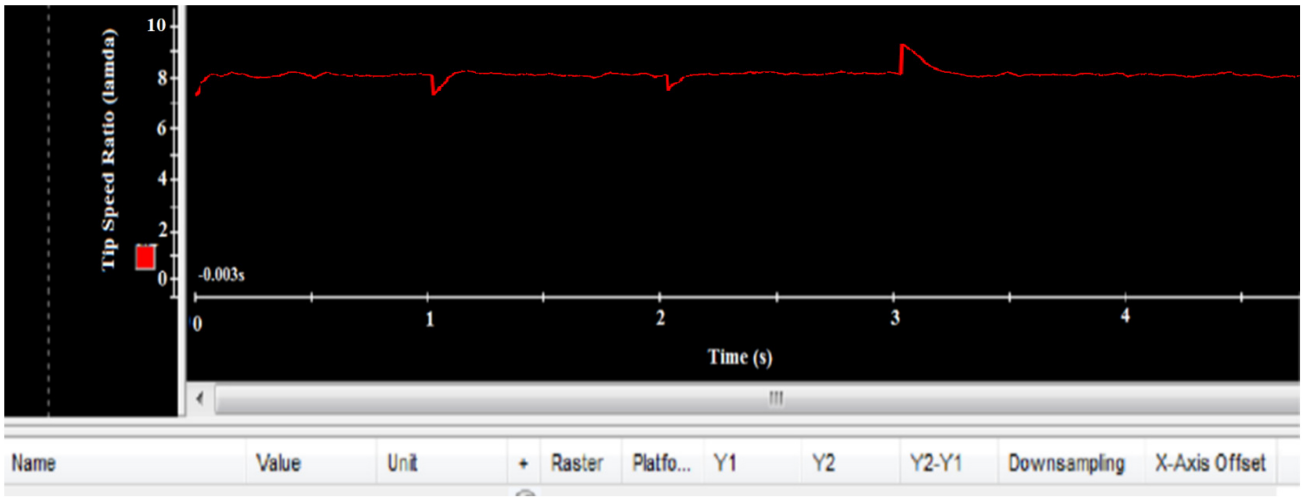
**Figure 26.** Real-time laboratory measured Power Coefficient using (**a**) PI controller, (**b**) AFLC, and (**c**) SO-AFLC.

The measured DC-link voltage responses are presented in Figure 28. The proposed SO-AFLC effectively regulates the DC-link voltage despite successive wind-speed disturbances, restoring the reference value more rapidly than both the PI and AFLC controllers at t = 2 s and t = 3 s. In addition to reducing voltage oscillations, the proposed controller improves transient stability and maintains a smoother voltage profile throughout the experiment.

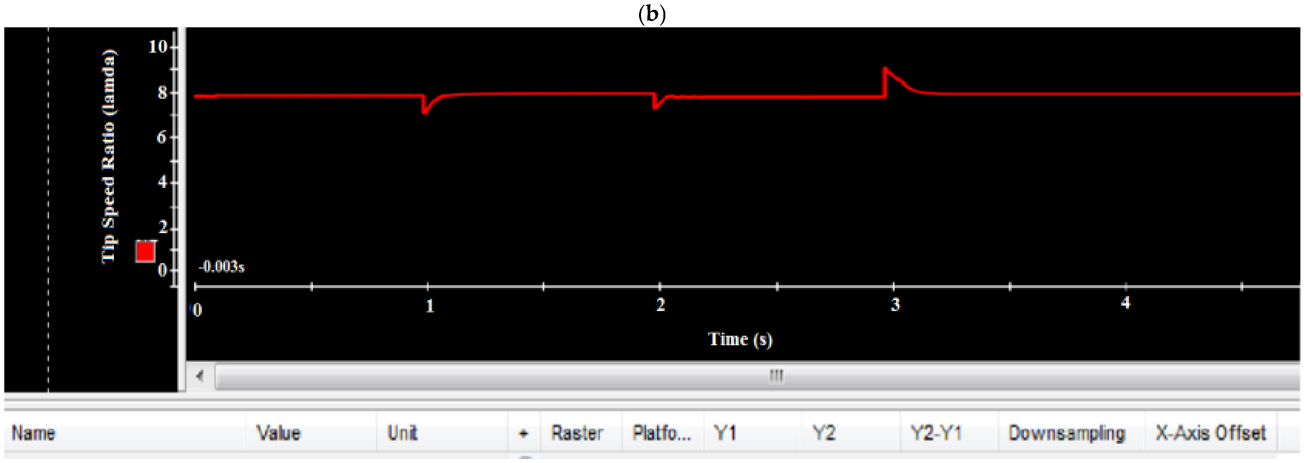



(**a**)

**Figure 27.** *Cont.*




(**b**)

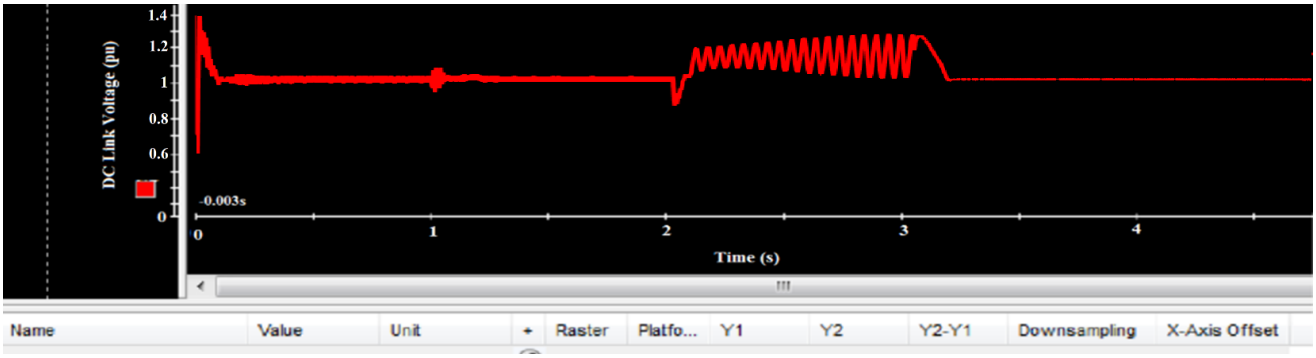



(**c**)

**Figure 27.** Real-time laboratory measured tip speed ratio using (**a**) PI controller, (**b**) AFLC, and (**c**) SO-AFLC.

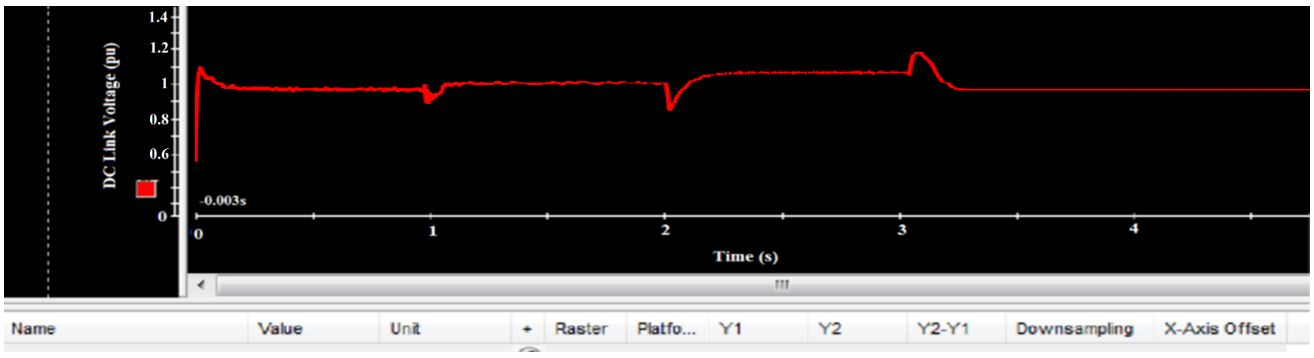
### *5.2. Case 2: Random Wind Speed Profile*

In Case II, to evaluate the controller performance under varying operating conditions, the wind speed was emulated using a DC motor and varied in a realistic wind manner as illustrated in Figure 29. This experimental scenario was designed to replicate realistic wind fluctuations and assess the dynamic response and robustness of the proposed control strategy.

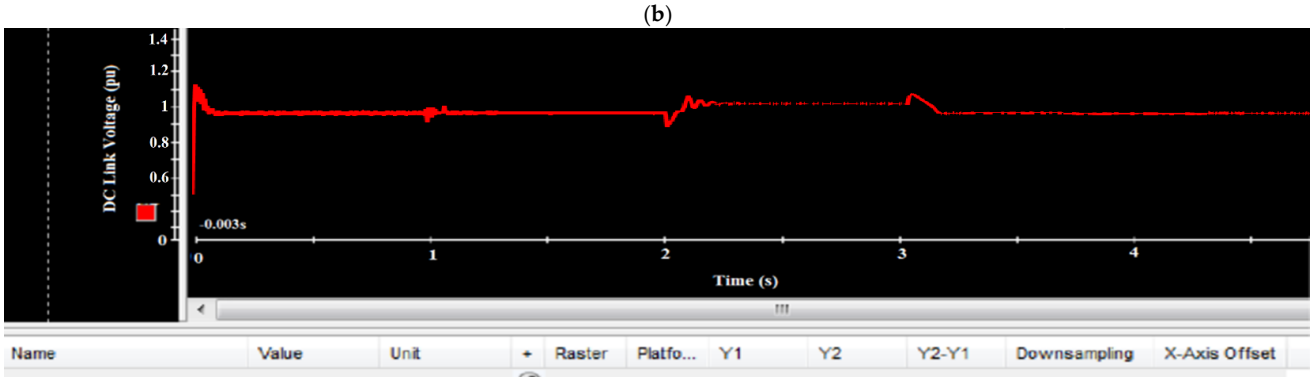



(**a**)

**Figure 28.** *Cont.*




(**b**)




(**c**)

**Figure 28.** Real-time laboratory measured DC link voltage between GCC and MSC using (**a**) PI controller, (**b**) AFLC, and (**c**) SO-AFLC.

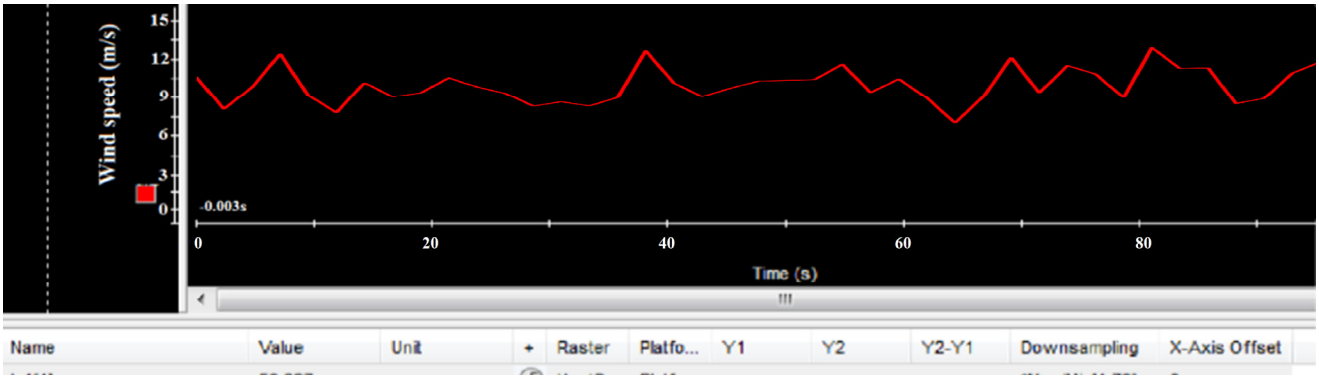



**Figure 29.** Real-time laboratory random wind speed profile.

Figure 30 illustrates the PMSG rotor-speed responses. Both AFLC and SO-AFLC demonstrate improved tracking accuracy compared with the PI controller, while SO-AFLC provides the fastest dynamic response. Quantitatively, the proposed controller improves rotor-speed tracking performance by 54.83% relative to PI and by 9.47% relative to AFLC.

Figure 31 presents the power coefficient ($C_p$) responses obtained using the three control strategies. In all cases, ($C_p$) is regulated around its optimal value of 0.48. Both AFLC and SO-AFLC provide improved performance compared with the conventional PI controller, with SO-AFLC achieving the best overall response. Moreover, the proposed SO-AFLC reduces the steady-state error in the $C_p$ response by 10.23% compared with AFLC and by 57.26% compared with PI.

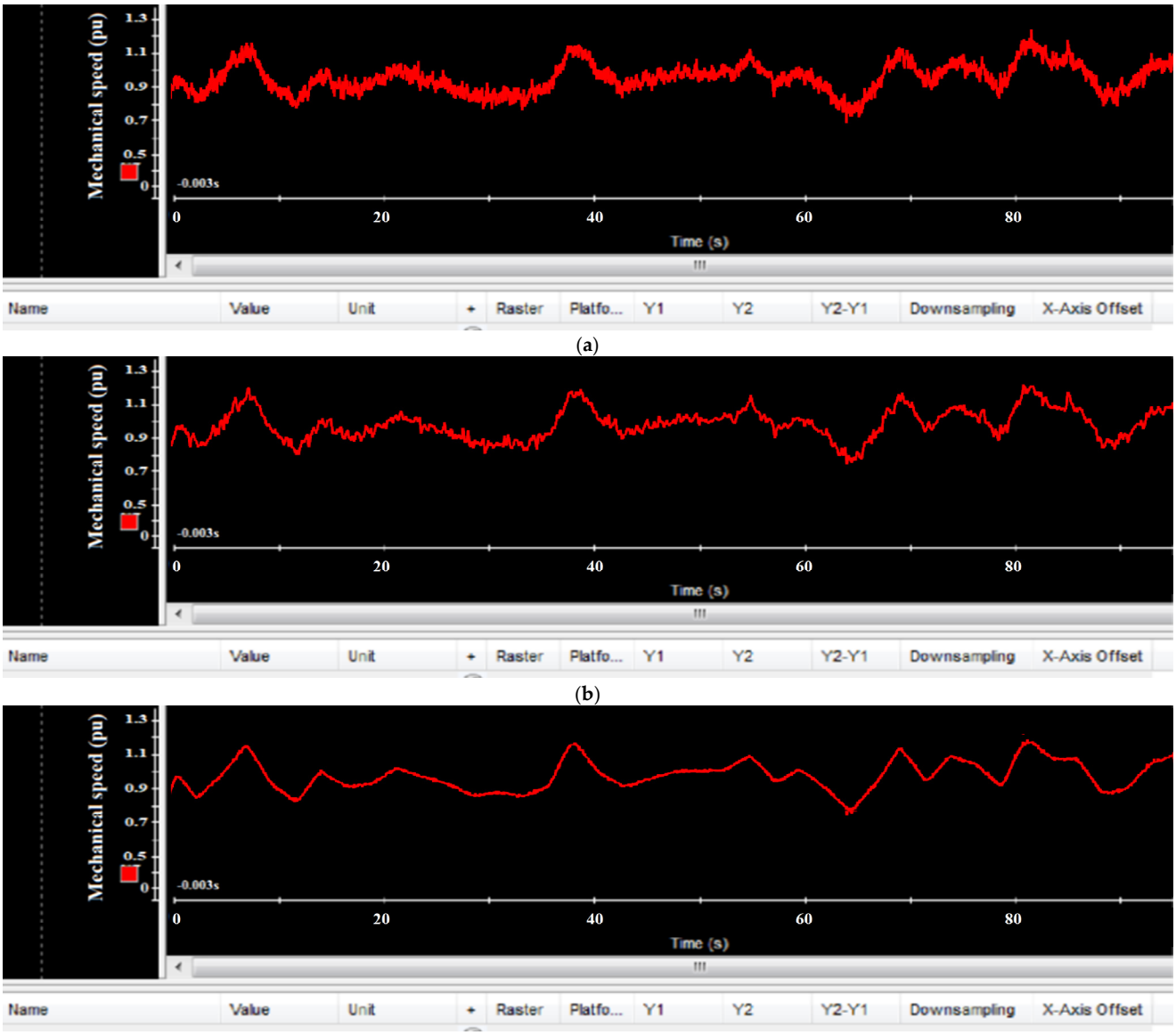



**Figure 30.** Real-time laboratory measured rotational speed using (**a**) PI controller, (**b**) AFLC, and (**c**) SO-AFLC.

The tip-speed-ratio responses are presented in Figure 32, with all controllers regulating (lambda) toward its optimal value of 8.1. The SO-AFLC achieves superior steady-state accuracy compared with AFLC and PI. Both SO-AFLC and AFLC reduce the ripple, with SO-AFLC providing a slightly better response.

Figure 33 presents the DC-link voltage response between the machine-side converter (MSC) and grid-side converter (GCC). The GCC effectively maintains the DC-link voltage around its reference value despite variations in wind speed. Under high-wind-speed conditions, both SO-AFLC and AFLC reduce the resulting overshoot, with SO-AFLC providing a slightly better response. In addition, SO-AFLC achieves the lowest steady-state error among the three controllers, demonstrating its superior capability to maintain stable DC-link voltage regulation under varying operating conditions.

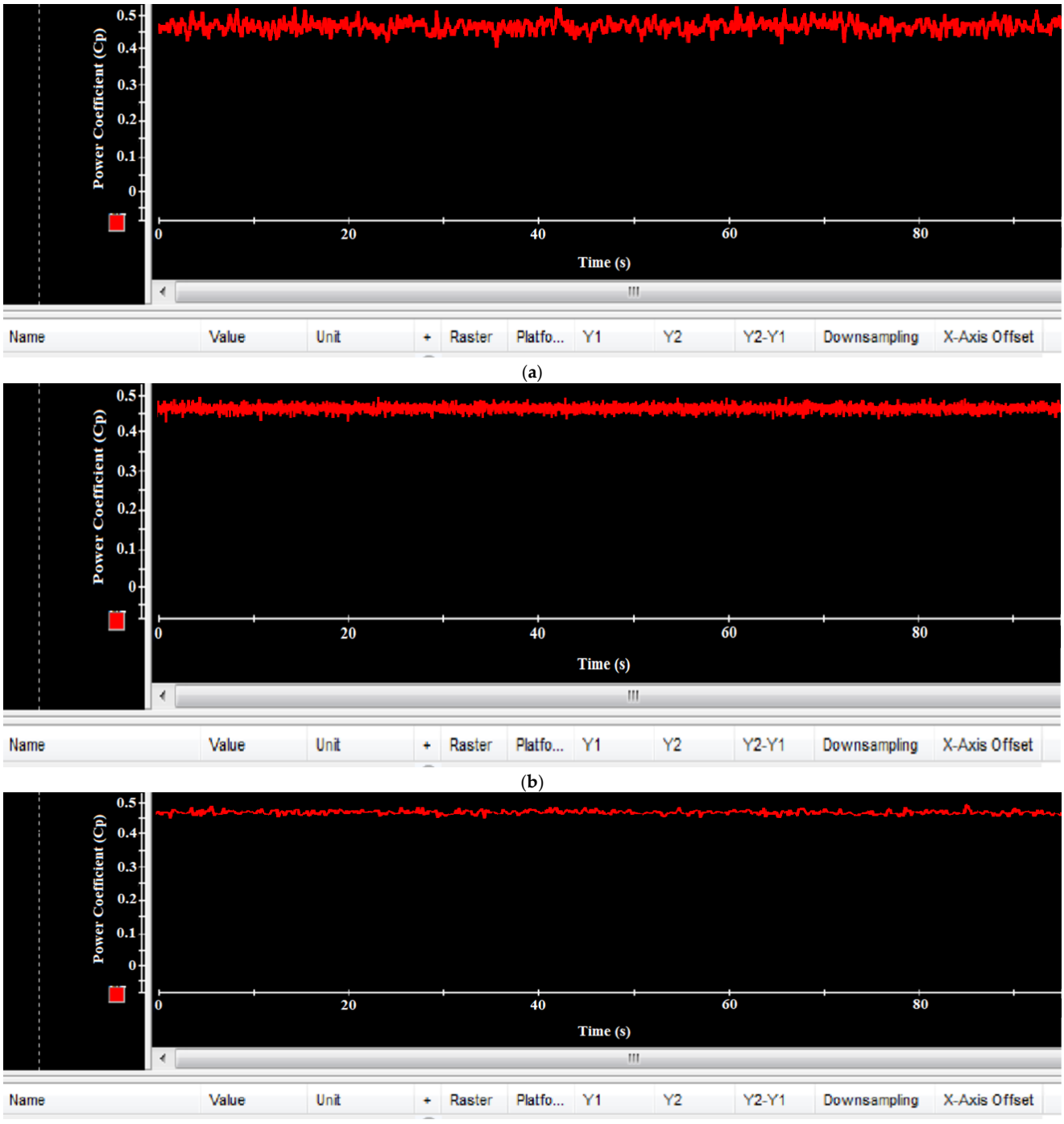



**Figure 31.** Real-time laboratory measured Power Coefficient (Cp) using (**a**) PI controller, (**b**) AFLC, and (**c**) SO-AFLC.

The co-simulation findings further validate the experimental hardware findings through comparison with the corresponding Simulink/MATLAB simulation outcomes. A strong correlation between the simulation and hardware findings corroborates the effectiveness and dependability of the suggested control approach. The results demonstrate that the SO-AFLC provides superior dynamic performance, characterized by enhanced tracking accuracy, faster system response, and improved disturbance rejection compared with the AFLC and PI controllers. Moreover, the proposed SO-AFLC significantly suppresses oscillatory behavior and minimizes tracking errors, resulting in a more stable and robust system operation under varying operating conditions.

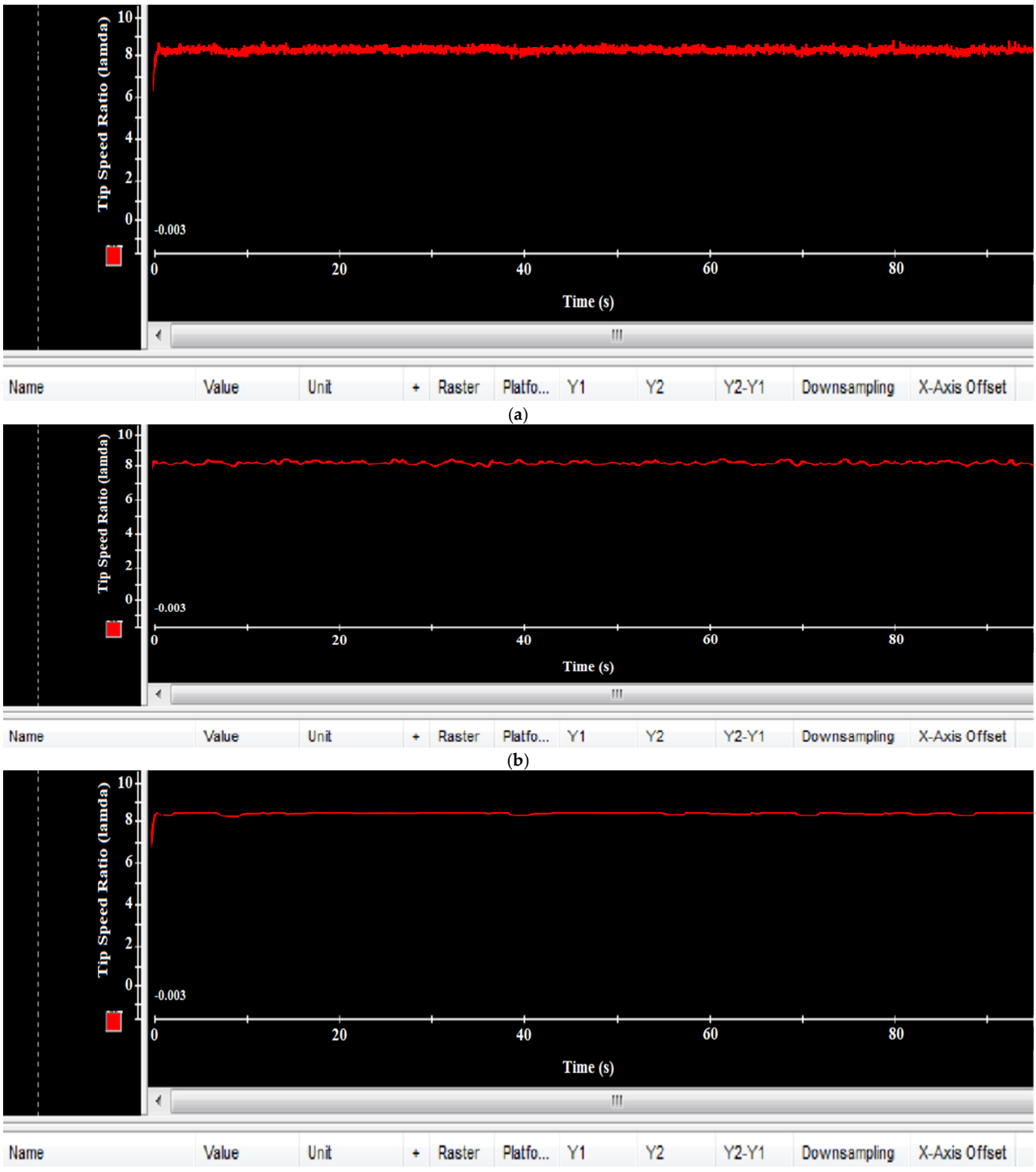



**Figure 32.** Real-time laboratory measured tip speed ratio using (**a**) PI controller, (**b**) AFLC, and (**c**) SO-AFLC.

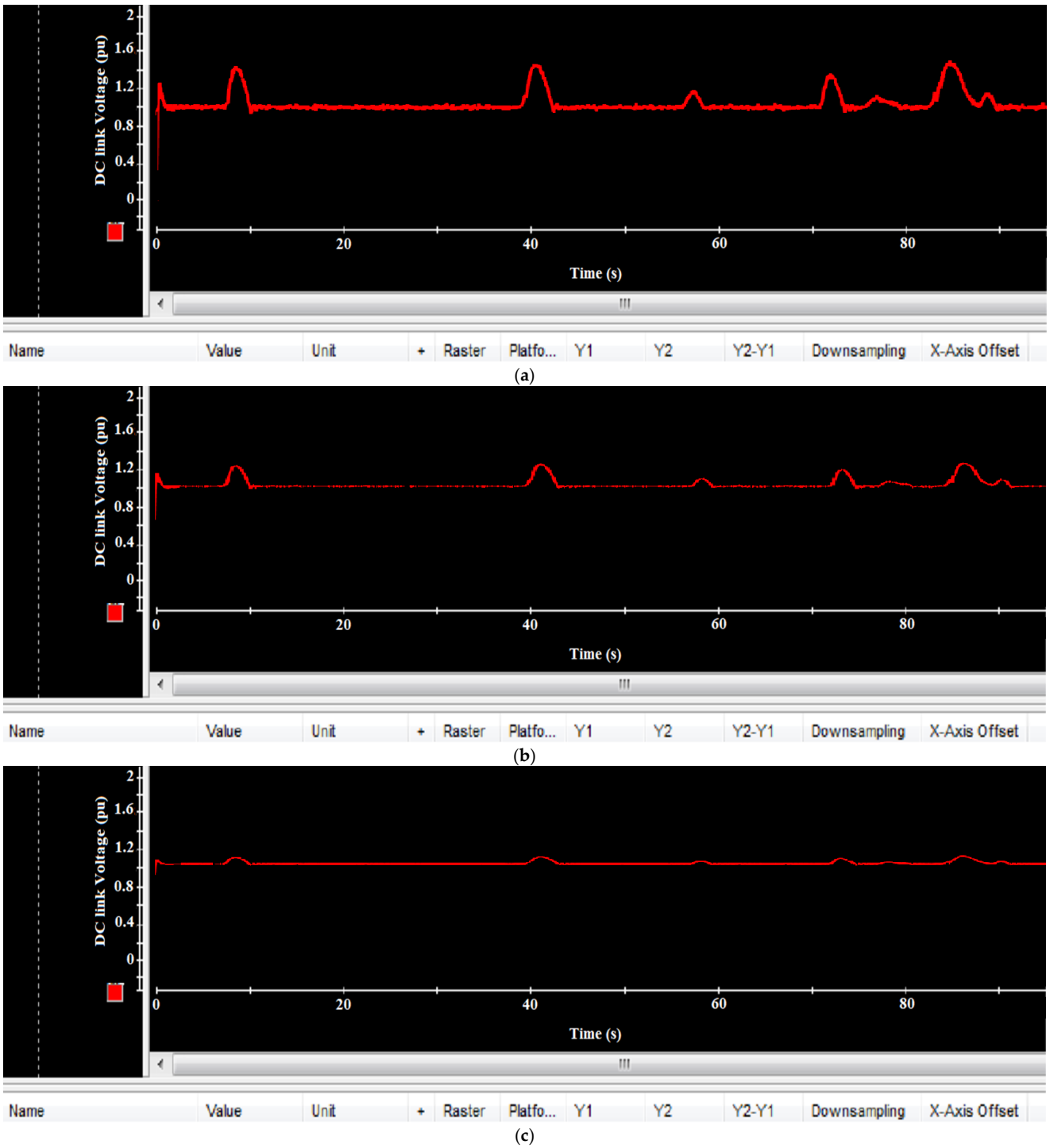



**Figure 33.** Real-time laboratory measured DC link voltage between GCC and MSC using (**a**) PI controller, (**b**) AFLC, and (**c**) SO-AFLC.

## 6. Conclusions

This study proposed and experimentally validated a SO-AFLC to enhance the control performance of a PMSG-based WECS operating under both abrupt wind variations and realistic wind conditions. The proposed strategy simultaneously addresses DC-link voltage regulation, MPPT, and reactive power control within a unified framework, resulting in enhanced dynamic stability and more accurate reference tracking. Extensive simulation studies together with real-time laboratory implementation demonstrated the effectiveness of the proposed controller over conventional PI and first-order adaptive fuzzy logic con-

trollers. During step wind speed changes, the SO-AFLC provided faster transient recovery, lower overshoot, shorter settling time, and negligible steady-state error for key operating variables, including the power coefficient, tip-speed ratio, rotor speed, mechanical power, DC-link voltage, and reactive power. The experimental results closely matched the simulation outcomes, confirming the practicality and superiority of the proposed control strategy for real-time applications. The controller was further evaluated using measured wind speed data from Ras Gharib in the Gulf of Suez, Egypt, where continuously varying wind conditions were considered. Even under these stochastic operating scenarios, the SO-AFLC maintained excellent tracking capability and strong robustness against wind fluctuations. Under step wind speed, Simulation evaluation showed improvements in rotor-speed tracking of 53.26% and 36.98% compared with the PI and AFLC controllers, respectively. However, experimental evaluation showed that the SO-AFLC improves rotor-speed tracking performance by 52.65% relative to PI and by 8.29% relative to AFLC. In addition, the proposed approach reduced the average of IAEs by 21.36% relative to the PI regulator and 9.15% relative to the AFLC, demonstrating its ability to minimize tracking deviations while improving overall control quality. The combined simulation and experimental findings verify that the proposed SO-AFLC enhances disturbance rejection, suppresses oscillatory behavior, improves damping characteristics, and increases energy extraction significantly. The proposed controller achieves improved dynamic performance while maintaining real-time implementation on the employed dSPACE DS1104 platform. Consequently, the proposed controller represents a reliable and practical solution for high-performance PMSG-based WECSs and is well suited for future deployment in grid-connected renewable energy applications.

Future research will investigate the use of the suggested control approach to hybrid renewable energy systems, coordinated grid-support services, and fault-tolerant operation under severe grid disturbances and varying network conditions.

**Author Contributions:** Conceptualization, A.M.I. and B.E.E.; methodology, B.E.E., A.M.I. and M.M.I.; investigation, A.M.I. and H.S.S.A.; Validation, A.M.I. and M.M.I.; writing—original draft preparation, A.M.I. and H.S.S.A.; writing—review and editing, M.M.I., A.M.I. and B.E.E.; Funding Acquisition, M.M.I. and H.S.S.A. All authors have read and agreed to the published version of the manuscript.

**Funding:** This research received no external funding.

**Data Availability Statement:** The original contributions presented in the study are included in the article, further inquiries can be directed at the corresponding author.

**Conflicts of Interest:** The authors declare no conflicts of interest.

## Nomenclature

| | |
|---|---|
| $\beta$ | Blade pitch angle (°) |
| $\lambda$ | Tip speed ratio (TSR) |
| R | Blade radius (m) |
| $\rho$ | Air density (kg/m$^3$) |
| $v_w$ | Wind speed (m/s) |
| $C_p$ | Power coefficient |
| $v_{sd}$ and $v_{sq}$ | The stator voltage components along the d-q axes, respectively; |
| $I_{sd}$ and $I_{sq}$ | The corresponding stator current components; |
| $R_s$ | The stator winding resistance; |
| $\omega_e$ | The electrical angular speed of the generator; |

| | |
|---|---|
| $L_q$ and $L_d$ | d-q axis inductance, |
| $\psi_m$ | Permanent the flux linkages. |
| $Q_g$ | Reactive Power injected to grid |
| $p$ | The number of pole pairs |

## References


1. Song, D.; Yang, Y.; Zheng, S.; Deng, X.; Yang, J.; Su, M.; Tang, W.; Yang, X.; Huang, L.; Joo, Y.H. New perspectives on maximum wind energy extraction of variable-speed wind turbines using previewed wind speeds. *Energy Convers. Manag.* **2020**, *206*, 112496. [CrossRef]
2. Song, D.; Liu, J.; Yang, J.; Su, M.; Yang, S.; Yang, X.; Joo, Y.H. Multi-objective energy-cost design optimization for the variable-speed wind turbine at high-altitude sites. *Energy Convers. Manag.* **2019**, *196*, 513–524. [CrossRef]
3. Yesilbudak, M. Implementation of novel hybrid approaches for power curve modeling of wind turbines. *Energy Convers. Manag.* **2018**, *171*, 156–169. [CrossRef]
4. Yin, M.; Xu, Y.; Shen, C.; Liu, J.; Dong, Z.Y.; Zou, Y. Turbine stability-constrained available wind power of variable speed wind turbines for active power control. *IEEE Trans. Power Syst.* **2016**, *32*, 2487–2488. [CrossRef]
5. Abdelrahem, M.; Hackl, C.M.; Kennel, R. Finite position set-phase locked loop for sensorless control of direct-driven permanent-magnet synchronous generators. *IEEE Trans. Power Electron.* **2017**, *33*, 3097–3105. [CrossRef]
6. Chen, H.; Xu, D.; Deng, X. Control for power converter of small-scale switched reluctance wind power generator. *IEEE Trans. Ind. Electron.* **2020**, *68*, 3148–3158. [CrossRef]
7. Muyeen, S.M.; Takahashi, R.; Murata, T.; Tamura, J. A variable speed wind turbine control strategy to meet wind farm grid code requirements. *IEEE Trans. Power Syst.* **2009**, *25*, 331–340. [CrossRef]
8. Jeon, H.; Kang, Y.C.; Park, J.W.; Lee, Y.I. PI control loop–based frequency smoothing of a doubly-fed induction generator. *IEEE Trans. Sustain. Energy* **2021**, *12*, 1811–1819. [CrossRef]
9. Mohamed, R.G.; Ebrahim, M.A.; Alaas, Z.M.; Ahmed, M.M.R. Optimal energy harvesting of large-scale wind farm using marine predators algorithm. *IEEE Access* **2022**, *10*, 24995–25004. [CrossRef]
10. Zhang, Z.; Li, Z.; Kazmierkowski, M.P.; Rodríguez, J.; Kennel, R. Robust predictive control of three-level NPC back-to-back power converter PMSG wind turbine systems with revised predictions. *IEEE Trans. Power Electron.* **2018**, *33*, 9588–9598. [CrossRef]
11. Sattar, A.; Al-Durra, A.; Caruana, C.; Debouza, M.; Muyeen, S.M. Testing the performance of battery energy storage in a wind energy conversion system. *IEEE Trans. Ind. Appl.* **2020**, *56*, 3196–3206. [CrossRef]
12. Tang, X.; Yin, M.; Shen, C.; Xu, Y.; Dong, Z.Y.; Zou, Y. Active power control of wind turbine generators via coordinated rotor speed and pitch angle regulation. *IEEE Trans. Sustain. Energy* **2018**, *10*, 822–832. [CrossRef]
13. Mousavi, Y.; Bevan, G.; Küçükdemiral, I.B.; Fekih, A. Maximum power extraction from wind turbines using a fault-tolerant fractional-order nonsingular terminal sliding mode controller. *Energies* **2021**, *14*, 5887. [CrossRef]
14. Ihedrane, Y.; Bekkali, C.E.; Bossoufi, B.; Bouderbala, M. Control of power of a DFIG generator with MPPT technique for wind turbines variable speed. In *Modeling, Identification Control Methods in Renewable Energy Systems*; Springer: Singapore, 2019; pp. 105–129.
15. Pande, J.; Nasikkar, P. A Maximum Power Point Tracking Technique for a Wind Power System Based on the Trapezoidal Rule. *Energies* **2023**, *16*, 2799. [CrossRef]
16. Soliman, M.A.; Hasanien, H.M.; Al-Durra, A.; Debouza, M. High performance frequency converter controlled variable-speed wind generator using linear-quadratic regulator controller. *IEEE Trans. Ind. Appl.* **2020**, *56*, 5489–5498. [CrossRef]
17. Majout, B.; Bossoufi, B.; Bouderbala, M.; Masud, M.; Al-Amri, J.F.; Taoussi, M.; El Mahfoud, M.; Motahhir, S.; Karim, M. Improvement of PMSG-Based Wind Energy Conversion System Using Developed Sliding Mode Control. *Energies* **2022**, *15*, 1625. [CrossRef]
18. Salem, A.A.; Aldin, N.A.N.; Azmy, A.M.; Abdellatif, W.S. Implementation and validation of an adaptive fuzzy logic controller for MPPT of PMSG-based wind turbines. *IEEE Access* **2021**, *9*, 165690–165707. [CrossRef]
19. Gulzar, M.M.; Sibtain, D.; Murtaza, A.F.; Murawwat, S.; Saadi, M.; Jameel, A. Adaptive fuzzy based optimized proportional-integral controller to mitigate the frequency oscillation of multi-area photovoltaic thermal system. *Int. Trans. Electr. Energy Syst.* **2021**, *31*, e12643. [CrossRef]
20. Zeb, K.; Ali, Z.; Saleem, K.; Uddin, W.; Javed, M.; Christofides, N. Indirect field-oriented control of induction motor drive based on adaptive fuzzy logic controller. *Electr. Eng.* **2017**, *99*, 803–815. [CrossRef]
21. Zamzoum, O.; Derouich, A.; Motahhir, S.; El Mourabit, Y.; El Ghzizal, A. Performance analysis of a robust adaptive fuzzy logic controller for wind turbine power limitation. *J. Clean. Prod.* **2020**, *265*, 121659. [CrossRef]

22. Teklehaimanot, Y.K.; Ubochi, B.C.; Ale, T.O.; Akingbade, K.F. Optimal FOPI-MPPT Controller for Grid-Connected DFIG Wind Turbines via PSO. *Arab. J. Sci. Eng.* **2025**, *51*, 8429–8445. [CrossRef]
23. Elnaghi, B.E.; Ismaiel, A.M.; Ismail, M.M.; Zedan, H.A.; Salem, A.A. Experimental validation of an adaptive fuzzy logic controller for MPPT of grid connected PV system. *Sci. Rep.* **2025**, *15*, 27173. [CrossRef] [PubMed]
24. Hocini, Y.; Allali, A.; Boulouiha, H.M. Power fuzzy adaptive control for wind turbine. *Int. J. Electr. Comput. Eng. (IJECE)* **2020**, *10*, 5262–5273. [CrossRef]
25. Soliman, M.A.; Hasanien, H.M.; Azazi, H.Z.; El-Kholy, E.E.; Mahmoud, S.A. An adaptive fuzzy logic control strategy for performance enhancement of a grid-connected PMSG-based wind turbine. *IEEE Trans. Ind. Inform.* **2018**, *15*, 3163–3173. [CrossRef]
26. Farag, W.; El-Hosary, H.; El-Metwally, K.; Kamel, A. Design and implementation of a variable-structure adaptive fuzzy-logic yaw controller for large wind turbines. *J. Intell. Fuzzy Syst.* **2016**, *30*, 2773–2785. [CrossRef]
27. Biyazne, L.W.; Tuka, M.B.; Abebe, Y.M.; Wellhöfer, A. Enhancing MPPT performance of a grid-connected Doubly-Fed induction generator-based wind power plant using hybrid ANFIS-PI control strategy. *Sci. Rep.* **2026**, *16*, 5732. [CrossRef] [PubMed]
28. Hosny, M.; Marei, M.I.; Mohamad, A.M.I. Adaptive hybrid virtual inertia controller for PMSG-based wind turbine based on fuzzy logic control. *Sci. Rep.* **2025**, *15*, 3757. [CrossRef] [PubMed]
29. Ali, M.; Ahmad, M.; Koondhar, M.A.; Akram, M.S.; Verma, A.; Khan, B. Maximum power point tracking for grid-connected photovoltaic system using Adaptive Fuzzy Logic Controller. *Comput. Electr. Eng.* **2023**, *110*, 108879. [CrossRef]
30. Hasanien, H.M.; Matar, M. A fuzzy logic controller for autonomous operation of a voltage source converter-based distributed generation system. *IEEE Trans. Smart Grid* **2014**, *6*, 158–165. [CrossRef]
31. Elnaghi, B.E.; Ismaiel, A.M.; Abdel-Kader, F.E.S.; Abelwhab, M.N.; Mohammed, R.H. Validation of energy valley optimization for adaptive fuzzy logic controller of DFIG-based wind turbines. *Sci. Rep.* **2025**, *15*, 711. [CrossRef] [PubMed]
32. Chotikunnan, P.; Pititheeraphab, Y. Adaptive p control and adaptive fuzzy logic controller with expert system implementation for robotic manipulator application. *J. Robot. Control (JRC)* **2023**, *4*, 217–226. [CrossRef]
33. Chakraborty, A.; Maity, T. An adaptive fuzzy logic control technique for LVRT enhancement of a grid-integrated DFIG-based wind energy conversion system. *ISA Trans.* **2023**, *138*, 720–734. [CrossRef] [PubMed]
34. Aranizadeh, A.; Mirmozaffari, M.; Farahani, B.K. Maximizing wind turbine power generation through adaptive fuzzy logic control for optimal efficiency and performance. *Wind* **2025**, *5*, 4. [CrossRef]
35. Elnaghi, B.E.; Abelwhab, M.N.; Abdel-Kader, F.E.S.A.; Ismaiel, A.M.; Mohammed, R.H.; Dessouki, M.E. Experimental validation of second-order adaptive fuzzy logic controller for grid-connected DFIG wind power plant. *IEEE Access* **2023**, *11*, 135255–135271. [CrossRef]
36. Elnaghi, B.E.; Abelwhab, M.N.; Mohammed, R.H.; Abdel-Kader, F.E.S.; Ismaiel, A.M.; Dessouki, M.E. The validation and implementation of the second-order adaptive fuzzy logic controller of a double-fed induction generator in an oscillating water column. *Electronics* **2024**, *13*, 291. [CrossRef]
37. Saghafinia, A.; Ping, H.W.; Uddin, M.N.; Gaeid, K.S. Adaptive fuzzy sliding-mode control into chattering-free IM drive. *IEEE Trans. Ind. Appl.* **2015**, *51*, 692–701. [CrossRef]
38. El-Sousy, F.F.M. Adaptive dynamic sliding-mode control system using recurrent RBFN for high-performance induction motor servo drive. *IEEE Trans. Ind. Informat.* **2013**, *9*, 1922–1936. [CrossRef]
39. Kochetkov, S.; Krasnova, S.A.; Utkin, V.A. The new second-order sliding mode control algorithm. *Mathematics* **2022**, *10*, 2214. [CrossRef]
40. Chen, J.; Shuai, Z.; Zhang, H.; Zhao, W. Path following control of autonomous four-wheel-independent-drive electric vehicles via second-order sliding mode and nonlinear disturbance observer techniques. *IEEE Trans. Ind. Electron.* **2021**, *68*, 2460–2469. [CrossRef]
41. Ding, S.; Park, J.H.; Chen, C.-C. Second-order sliding mode controller design with output constraint. *Automatica* **2020**, *112*, 108704. [CrossRef]
42. Kumar, G.A.; Shivashankar. Optimal power point tracking of solar and wind energy in a hybrid wind solar energy system. *Int. J. Energy Environ. Eng.* **2022**, *13*, 77–103. [CrossRef]
43. Mishra, R.; Saha, T.K. Predictive Power Control of PMSG based WECS: Development and Implementation for Smooth Grid Synchronisation, Balanced and Unbalanced Grid. *Math. Comput. Simul.* **2024**, *215*, 323–337. [CrossRef]
44. Okedu, K.E.; Barghash, H. Enhancing the Transient State Performance of Permanent Magnet Synchronous Generator Based Variable Speed Wind Turbines Using Power Converters Excitation Parameters. *Front. Energy Res.* **2021**, *9*, 655051. [CrossRef]
45. Syahputra, R.; Soesanti, I. Performance improvement for small-scale wind turbine system based on maximum power point tracking control. *Energies* **2019**, *12*, 3938. [CrossRef]

46. Belkhier, Y.; Achour, A. Passivity-based voltage control design of grid connected wind turbine with PMSG. In *Proceedings of the 2020 IEEE ANDESCON, Quito, Ecuador, 13–16 October 2020*; IEEE: New York, NY, USA, 2020; pp. 1–5.
47. Ahmed, A.S. Investigation of wind characteristics and wind energy potential at Ras Ghareb, Egypt. *Renew. Sustain. Energy Rev.* **2011**, *15*, 2750–2755. [CrossRef]

**Disclaimer/Publisher's Note:** The statements, opinions and data contained in all publications are solely those of the individual author(s) and contributor(s) and not of MDPI and/or the editor(s). MDPI and/or the editor(s) disclaim responsibility for any injury to people or property resulting from any ideas, methods, instructions or products referred to in the content.